Paleoenvironmental change in a precession-paced succession across the onset of the Messinian salinity crisis: Insight from element geochemistry and molecular fossils

Paleoenvironmental change in a precession-paced succession across the onset of the Messinian salinity crisis: insight from element geochemistry and molecular fossils

Marcello Natalicchio[1*], Francesco Dela Pierre[1*], Daniel Birgel[2], Hans Brumsack[3], Giorgio Carnevale[1], Rocco Gennari[1], Susanne Gier[4], Francesca Lozar[1], Luca Pellegrino[1], Mathia Sabino[2], Bernhard Schnetger[3] and Jörn Peckmann[2]

[1]Dipartimento di Scienze della Terra, Università degli Studi di Torino, Torino, Italy

[2] Institut für Geologie, Centrum für Erdsystemforschung und Nachhaltigkeit, Universität Hamburg, Hamburg, Germany

[3] Institut für Chemie und Biologie des Meeres, Universität Oldenburg, Oldenburg, Germany

[4] Department für Geodynamik und Sedimentologie, Universität Wien, Wien, Austria

[*]corresponding authors

E-mail: marcello.natalicchio@unito.it, francesco.delapierre@unito.it

Abstract

In marginal Mediterranean sub-basins, the early phase of the Messinian salinity crisis (MSC) is recorded by cyclic successions of gypsum and shales, which in deeper parts of the sub-basins make lateral transition into organic-rich shales, marls, and carbonates. The cyclic stacking pattern of the gypsum-bearing sequences is assumed to reflect periodic paleoenvironmental change induced by precession-driven climate perturbations, with the assumption that shales reflect humid climate (precession minima) while gypsum reflects arid conditions (precession maxima). However, this correlation has not been verified to date, mostly because of the scarcity of microfossils, the most commonly used tools for the reconstruction of precession-driven paleoenvironmental change. Such change can, instead, be reconstructed through the study of the deeper water counterparts of gypsum (marly and carbonate layers) with geochemical indicators (major and trace elements, molecular fossils), which provide insight on climate and aquatic productivity. We used this approach to study a section from the Piedmont Basin (NW Italy) where the onset of the MSC is archived in a sequence of organic-rich sediments. This sequence displays distinct lithological cyclicity, evidenced by the repetition of couplets of organic-rich shales and marls, either bioturbated (in the pre-MSC part of the section) or laminated (during the MSC). The influence of orbitally-driven (precession) climate oscillations is demonstrated by fluctuations of Ti/Al, Si/Al, Mg/Al, K/Al, Zr/Al, and Ba/Al ratios that are in phase with lithological cyclicity. These fluctuations are interpreted to reflect alternation of humid (shales, deposited during precession minima) and arid (bioturbated and laminated marls, deposited during precession maxima) phases, dominated by fluvial and aeolian transport of detrital material, respectively. The cyclicity of the element ratios is mirrored by changes in organic carbon content and molecular fossil inventory. In particular, the distribution of long-chain *n*-alkanes and their degree of preservation reveal that humid phases at times of precession minima were typified

by the maximum input of degraded terrestrial organic matter driven by enhanced riverine runoff, which promoted water column stratification. Coeval increase in Ba content, a common paleoproductivity proxy, agrees with enhanced nutrient supply during humid periods, promoting phases of eutrophication in the basin. Lithological and geochemical changes are observed in MSC sediments deposited at times of precession maxima, evidenced by the replacement of pre-MSC bioturbated marls by laminated marls rich in filamentous fossils corresponding to the remains of probable colorless sulfide-oxidizing bacteria. Such changes reflect an intensification of water column stratification after the onset of the MSC, possibly related to the combined effect of persistent freshwater inflow and basin isolation, preluding the advent of gypsum precipitation.

Keywords:
Lithological cyclicity, Major and trace elements, Terrestrial organic matter, Fluvial and aeolian transport, Water column stratification

1. Introduction

During the Messinian, the Mediterranean Sea was progressively isolated from the Atlantic Ocean by the gradual tectonic uplift of the Betic and Rifian gateways (e.g., Duggen et al., 2003; Garcia-Castellanos and Villaseňor, 2011; Flecker et al., 2015; Capella et al., 2016). This trend was superposed to long (eccentricity) and short (precession) orbitally-driven climate perturbations, the effects of which were dramatically amplified because of limited water exchange with the Atlantic Ocean. The sedimentary products of the combined effects of tectonic restriction and astronomical forcing are cyclic successions of organic-rich shales, diatomites, and marls, deposited on the Mediterranean Sea bottom starting at about 7.1 Ma (Krijgsman et al., 1999; Negri et al., 1999; Sierro et al., 2003; Perez-Folgado et al.,

2003; Kouwenhoven et al., 2006; Hilgen et al., 2007; Roveri et al., 2014; Gennari et al., 2018). The isolation of the Mediterranean culminated in the extensive deposition of evaporites during the Messinian salinity crisis (MSC; 5.97-5.33 Ma; Manzi et al., 2013), when the basin was transformed into a giant salina (Hsü et al., 1977; Cita et al., 1978; Roveri et al., 2014; Flecker et al., 2015; Fig. 1A). The onset of the MSC is considered to represent a synchronous event throughout the Mediterranean (Manzi et al., 2013). In shallow marginal sub-basins (i.e., at a paleodepth < 200 m; Roveri et al., 2014), this event is marked by the deposition of the Primary Lower Gypsum unit (Roveri et al., 2008), which is characterized by distinct lithological cyclicity defined by shale-gypsum couplets. These evaporites make lateral transition into cyclic sequences of organic-rich sediments and carbonate layers, which were deposited in basins of intermediate to deep water depths (i.e., > 200 m; Manzi et al., 2007; Dela Pierre et al., 2011, 2012; Gennari et al., 2013, 2018; Lozar et al., 2018). Apparently, the formation of gypsum in these deep water basins was hampered by bottom oxygen depletion coupled with an intense bacterial sulfate reduction, responsible for decreasing sulfate concentration and consequent undersaturation with respect to gypsum (Bąbel, 2007; De Lange and Krijgsman, 2010).

Cyclic paleoenvironmental change induced by precession-driven climate perturbations have been extensively documented for pre-MSC sequences based on calcareous microfossil assemblages (e.g., Hilgen and Krijgsman, 1999; Sierro et al., 2003; Kouwenhoven et al., 2006; Gennari et al., 2018; Lozar et al., 2018) and by variations in the $^{87}Sr/^{86}Sr$, $\delta^{13}C$, and $\delta^{18}O$ isotope ratios of the tests of planktic foraminifers (Modestou et al., 2017; Reghizzi et al., 2017). These studies demonstrated that the formation of organic-rich shales was related to enhanced preservation of organic carbon, favoured by water column stratification, bottom water stagnation and anoxia, resulting from enhanced riverine runoff at precession minima corresponding to insolation maxima. The envisioned mechanism was apparently somewhat

different from that governing the deposition of the younger and more extensively studied Pliocene and Pleistocene sapropels of the Mediterranean Sea (e.g., Wehausen and Brumsack, 1998; Nijenhuis and de Lange, 2000). The latter is regarded as the product of an additional nutrient supply and enhanced productivity (Schenau et al., 1999) triggered by increased riverine runoff of the Nile caused by the northward shift of the North African monsoon system (Gladstone et al., 2007; Marzocchi et al., 2015; Rohling et al., 2015).

In contrast, the influence of precessional forcing on the deposition of the Primary Lower Gypsum unit is not straightforward, especially due to the absence or scarcity of microfossils, related to the advent of hypersaline conditions not tolerated by the majority of eukaryotes (e.g., Bellanca et al. 2001). Actually, the hypothesis of the influence of precessional forcing on evaporite deposition is only supported by lithological cyclicity to date, based on the assumption that gypsum layers reflect more arid phases during precession maxima, while shales are assumed to be indicative of humid conditions during precession minima (Roveri et al., 2014; Simon et al., 2017). One possibility to investigate the influence of precessional forcing on MSC sequences is the analysis of the deeper water equivalents of the Primary Lower Gypsum unit. Such successions, which consist of organic-rich shales, marls, and carbonates, have received much less attention than their pre-MSC counterparts. In the absence or scarcity of body fossils, the paleoenvironmental and paleoclimatic change occurring across the onset of the MSC can be investigated in these successions through the study of inorganic and organic geochemical proxies, such as major and trace elements, providing insights on climate conditions and paleoproductivity (e.g., Wehausen and Brumsack, 1998; Calvert and Pedersen, 2007), and molecular fossils (lipid biomarkers) of terrestrial organic matter, reflecting climate-dependent change in terrestrial vegetation (e.g., Eglinton and Hamilton, 1963, Schefuß et al., 2003).We applied this approach to study an inferred precession-paced succession exposed in the Pollenzo section (Piedmont Basin, NW

123 Italy; Figs. 1A, B) at the northernmost offshoot of the Mediterranean. In this section the onset
124 of the MSC does not coincide with the base of the Primary Lower Gypsum unit, but it is
125 archived in a sequence of fine-grained sediments (organic-rich shales, marls, and carbonate
126 rich layers; Dela Pierre et al., 2011; 2012; Violanti et al., 2013; Lozar et al., 2018). We
127 complemented the study of inorganic and organic geochemical proxies with sedimentological
128 and petrographical data with the aim to monitor the mutual relationships between orbitally-
129 driven paleoenvironmental change at the precessional scale and the production, accumulation,
130 and final preservation of sediments and organic matter across the onset and the earliest phase
131 of the MSC. This study provides new constraints on the physical and chemical parameters of
132 the water column and the sedimentary environment across the onset of the MSC in a marginal
133 basin.
134
135 **2. The Pollenzo section**
136
137 *2.1. Geological and stratigraphical setting*
138 The Pollenzo section (44°41'08''N; 7°55'33''E) is located in the Piedmont Basin
139 (Fig. 1B), a wide wedge-top basin filled with Upper Eocene to Messinian sediments (Rossi et
140 al., 2009; Mosca et al., 2010; Rossi, 2017). The Messinian succession is exposed in the
141 southern (Langhe) and northern (Torino Hill-Monferrato) basin margins, whereas in the
142 depocentral zones it is buried below Pliocene and Quaternary deposits (Irace et al., 2005;
143 Dela Pierre et al., 2011). The succession starts with outer shelf to slope deposits, referred to
144 as the Sant'Agata Fossili Marls (Tortonian-lower Messinian; Sturani, 1973). This unit
145 displays cyclic stacking pattern evidenced by the rhythmic repetition of shale/marl couplets
146 (Lozar et al., 2010, 2018; Dela Pierre et al., 2011; 2012; Violanti et al., 2013). Abundance
147 fluctuations of calcareous microfossil assemblages allowed to assign the lithological cyclicity

148 to precessional forcing (Violanti et al., 2007; 2013; Lozar et al., 2018), with shales reflecting
149 warm and humid conditions during precession minima (insolation maxima) and marls
150 pointing to cool and arid climate during precession maxima (insolation minima). The
151 Sant'Agata Fossili Marls are followed, at the basin margins, by primary sulfate evaporites of
152 the Primary Lower Gypsum unit (Dela Pierre et al. 2011). The latter corresponds to the first
153 stage of the MSC (5.97-5.60 Ma; Manzi et al., 2013) and consists of lithologic cycles
154 composed of shale-gypsum couplets (Fig. 1C). No *in situ* primary evaporites are documented
155 in the buried depocentral zones, but seismic data show that their time equivalent sediments
156 are represented by shales (Irace et al., 2010).
157
158 *2.2 Identification of the onset of the MSC*
159 The identification of the onset of the MSC in the Pollenzo section is based on physical
160 stratigraphic and biostratigraphic data (Dela Pierre et al., 2011; Lozar et al., 2010, 2018;
161 Violanti et al., 2013). Physical stratigraphic correlation allowed reconstructing the lateral
162 facies transition between the shallow marginal area of the basin and the depocentral zone;
163 such transition is exposed on the southern sector of the Piedmont Basin (Dela Pierre et al.,
164 2011; Fig. 1B). Along the basin margins (Arnulfi section; Figs. 1B, C), six Primary Lower
165 Gypsum cycles were recognized, composed of bottom grown-selenite layers; the sixth bed
166 records a sharp facies change (i.e., the appearance of the branching selenite facies; Lugli et
167 al., 2010) and represents a distinct marker bed, referred to as the Sturani key-bed, which can
168 be physically correlated and mapped throughout most of the Piedmont Basin (Dela Pierre et
169 al., 2011). In the Pollenzo section, which is closer to the basin depocenter, only two gypsum
170 beds (Pg1 and Pg2, Fig. 1C) are present below the Sturani marker bed. The Pg1 and Pg2
171 gypsum beds overly seven lithologic cycles (Pm1-Pm7; Fig. 2) belonging to the Sant'Agata
172 Fossili Marls. Each cycle, about 3 m thick, is bipartite and consists of laminated organic-rich

shales followed by marls, with the latter hosting a carbonate-rich bed (Dela Pierre et al., 2012). Due to their position with respect to the Sturani key-bed, the uppermost three cycles of the Sant'Agata Fossili Marls (Pm5-7) were considered as the deeper water counterparts of the lower three cycles of the Primary Lower Gypsum unit deposited in marginal sectors (Dela Pierre et al., 2011; Fig. 1C). Consequently, the onset of the MSC (i.e., the time line at 5.971 Ma) has been identified in the Pollenzo section in cycle Pm5, at the base of the marly hemicycle, which corresponds to the base of the first gypsum bed in marginal setting (Fig. 1C). Biostratigraphic data are in accord with the physical stratigraphic correlation. In cycle Pm5, Lozar et al. (2018) have documented a peculiar sequence of calcareous nannofossil bioevents (abundance peak of *Sphenolithus abies*, followed by minor peaks of *Helicosphaera carteri* and *Umbilicosphaera rotula*), as well as the disappearance of planktic foraminifers > 125 μm (*Globigerina bulloides, Turborotalita quinqueloba, Neogloquadrina* spp. *Globigerinita* spp.; Violanti et al., 2013). These bioevents are reliable tool for the identification of the onset of the MSC, independently from the occurrence of evaporites (Gennari et al., 2018; Manzi et al., 2018). Finally, an additional tie point is represented by the last occurrence of *Turborotalita multiloba* (40% of its relative abundance in the > 125 μm fraction) in the marls of cycle Pm1 (Violanti et al., 2013), which has been also recorded at the top of cycle UA31 (i.e., four cycles below the MSC onset) in the astronomically-tuned Perales section (Sierro et al., 2001; Fig. 2).

Summarizing, four pre-MSC cycles (Pm1-Pm4) are identified in the Pollenzo section, followed by three MSC cycles (Pm5-Pm7; Fig. 2). The uppermost evaporite-free cycle (Pm7) is overlain by two gypsum-bearing cycles (Pg1 and Pg2; Figs. 1C, 2), which correspond to the 4th and 5th Primary Lower Gypsum cycles, immediately below the Sturani key-bed (6th Primary Lower Gypsum cycle; Fig. 1C).

198 ## 3. Material and methods

199

200 A total of 57 samples were taken from cycles Pm 3, 4, 5, 6, 7, and Pg1. Each sample
201 was split into two parts, one used for petrographical and mineralogical analyses, the other for
202 geochemical analyses.

203

204 ### *3.1 Petrography and mineralogy*

205 The samples were cut both parallel and perpendicular to bedding after epoxy
206 impregnation. 15 slabs and 21 thin sections from the most representative samples were
207 studied using transmitted, reflected, and UV light microscopy. Scanning electron microscopy
208 (SEM) analyses were performed on ten stubs for morphological analyses and on seven
209 polished carbon-coated thin sections for semiquantitative elemental analyses and
210 backscattered electron imagery, using a JSM-IT300LV scanning electron microscope
211 equipped with an energy-dispersive EDS Oxford Instrument Link System microprobe
212 (Department of Earth Sciences, University of Torino). X ray diffraction (XRD) analyses were
213 performed on twenty six bulk samples using a Panalytical X'Pert PRO diffractometer (CuKa
214 radiation, 40 kV, 40 mA, step size 0.0167, 5 s per step) at the Department of Geodynamics
215 and Sedimentology, University of Vienna. In addition, two samples representative of the
216 main studied facies were selected for clay mineral analyses. Oriented clay samples (<2 μm-
217 fraction) were prepared by pipetting 1 ml of suspension (10 mg/ml) onto a glass slide. They
218 were analyzed air-dried, saturated with Mg and K ions, and after saturation with ethylene
219 glycol and glycerol at 60° C for 12 h. Additionally, the samples were heated to 550° C. The
220 X-ray patterns were interpreted according to Moore and Reynolds (1997) and quantified
221 using the correction factors of Schultz (1964).

222

3.2 Total carbon and $CaCO_3$ contents

49 samples were analyzed at the Institute for Geology of the University of Hamburg to determine the total organic (TOC) and inorganic (TIC) carbon contents (Table 1 and Supplementary Table 1). The samples were dried and ground with a mortar and the resulting powder split in two aliquots. The first aliquot was heated to 1350° C and the total carbon (TC) content was measured using a LECO SC-144DR Carbon Analyzer equipped with an infrared detector. The second aliquot was heated first to 550° C for 5 h to remove the organic carbon and then heated to 1350° C to measure the inorganic carbon content (TIC); TOC contents were determined with the formula TOC = TC – TIC. A Synthetic Carbon Leco 502-029 (1.01 ± 0.02 carbon%) standard was measured prior to sample analyses. To express the TIC as percent calcium carbonate ($CaCO_3$), the following calculation was made: $CaCO_3$ = TIC × 8.33.

3.3 X-ray fluorescence analyses (XRF)

49 samples were analyzed using fused glass beads for major (Al, Si, Mg, K, Ti) and trace (Ba, Zr) elements using a wavelength-dispersive XRF spectrometer (Axios max®, Panalytical) at the Institute of Chemistry and Biology of the Marine Environment (University of Oldenburg). Analytical accuracy was checked with an in-house black shale reference material and international standard and was better than 1% for major elements and 5% for trace elements. The results are shown in Table 1 and Supplementary Table 1. Redox-sensitive elements (e.g., Mo and U; Algeo and Tribovillard, 2009) have also been analyzed, but only low contents close to detection limit were obtained, lacking distinct patterns. We, therefore, decided not to use these data. Because of the high concentration of Al in aluminosilicates, element/Al ratios were used for the assessment of the relative enrichment or depletion of specific elements in the samples (e.g., Brumsack, 2006; Calvert and Pedersen 2007)

248

Table 1
Average geochemical data (TOC, $CaCO_3$, major and trace elements) of the Pollenzo section samples

	Shales	Bioturbated marls	Laminated marls
TOC (wt%)	1.98	1.40	2.09
$CaCO_3$ (%)	18.3	33.8	34.8
XRF analyses			
SiO_2 (%)	41.3	35.1	30.0
Al_2O_3 (%)	13.0	10.3	9.0
MgO (%)	4.8	4.8	7.7
CaO (%)	12.4	19.9	20.1
Na_2O (%)	0.8	0.7	0.7
K_2O (%)	2.6	2.1	1.9
Ti_2O (%)	0.5	0.4	0.4
Ba (ppm)	604	296	248
Zr (ppm)	80	84	83
Ratios			
Ti/Al × 100	4.55	4.80	4.87
Mg/Al × 100	43.91	55.46	107.25
Si/Al	2.81	3.00	2.96
K/Al × 100	31.29	32.59	32.34
Zr/Al	11.67	16.15	19.94
Ba/Al	87.26	54.48	62.33
No. of samples	21	16	12

249

250

251 ### *3.4 Molecular fossils*

252 The detailed cleaning and extraction procedure applied in this study has been reported
253 elsewhere (Birgel et al., 2006). A total of 42 dry sediment samples were homogenized by
254 mortar and pestle. The muddy sediments were first saponified with 6% potassium hydroxide
255 in methanol using an ultrasonic bath to release carboxylic acids (2 hours at 80° C). The
256 saponification extract was collected in a separatory funnel. Then, the samples were extracted
257 by ultrasonication with dichloromethane (DCM):methanol (3:1). This procedure was repeated
258 until the extract became colorless. The combined extracts were treated with 10%
259 hydrochloric acid to pH 1 to transfer the free fatty acids to the organic solvent phase. For gas
260 chromatography (GC) analysis, each extract was cleaned by separation into *n*-hexane soluble

and DCM soluble fractions. The *n*-hexane fraction was further treated and separated via solid phase extraction using a Supelco glass cartridge (6 ml, 500 mg, DSC-NH2) into four fractions of increasing polarity: (1) hydrocarbons with 4 ml *n*-hexane, (2) ketones with 6 ml *n*-hexane:DCM (3:1, v/v), (3) alcohols with 7 ml DCM:acetone (9:1, v/v), (4) carboxylic acids with 8 ml 2% formic acid in DCM. Alcohols were derivatized to trimethyl silyl ethers by reacting them with a 1:1 mixture of pyridine and N,O-bis(trimethylsilyl)trifluoracetamide (BSTFA) at 70° C for 60 minutes. Free carboxylic acids were reacted with 1 ml 14% boron trifluoride in methanol at 70° C for 1 h to form fatty acid methyl esters. After cooling, the mixture was extracted four times with 2 ml *n*-hexane. Combined extracts were evaporated under a stream of nitrogen, and redissolved in *n*-hexane prior injection. The hydrocarbon fraction, the derivatized alcohol and carboxylic acid fractions were analyzed using coupled gas chromatography-mass spectrometry (GC-MS) with a Thermo Scientific Trace GC Ultra coupled to a Thermo Scientific DSQ II mass spectrometer. Quantification was performed using GC-flame ionization detection (GC-FID) with a Fisons Instruments GC 8000. Internal standards used were 5α-cholestane for hydrocarbons, 1-nonadecanol and DAGE *n*-C_{18}/*n*-C_{18} for the alcohols, and 2-Me-C_{18} fatty acid for the carboxylic acids. Both GC systems were equipped with a HP-5 MS UI fused silica column (30 m x 0.25 mm i.d., 0.25 µm film thickness). The carrier gas was helium for the GC-MS measurements and hydrogen for the GC-FID measurements. The GC temperature program for all fractions was: 50° C (3 min); from 50° C to 230° C (held for 3 minutes) at 25 °C/min; from 230° C to 325° C (held 20 min) at 6° C/min. Compound assignment was based on retention times and published mass spectral data.

Compound-specific carbon isotope analyses of all *n*-alkanes were performed with an Agilent 6890 gas chromatograph coupled with a Thermo Finnigan Combustion III interface to a Thermo Finnigan Delta Plus XL isotope ratio mass spectrometer (GC-irms) at the

Institute for Geology, University of Hamburg. The GC conditions were identical to those mentioned above for GC-FID and GC-MS analyses. Compound-specific carbon isotope values are given as $\delta^{13}C$ values in per mil (‰) relative to the Vienna Pedee Belemnite (V-PDB).

3.4.1 Lipid-based ratios

The Carbon Preference Index (CPI) was calculated for *n*-alkanes according to the formula below (Bray and Evans, 1961). It represents the predominance of odd over even *n*-alkanes of a certain length range.

$$\mathrm{CPI} = 0.5 \times \left(\frac{C_{25} + C_{27} + C_{29} + C_{31} + C_{33}}{C_{24} + C_{26} + C_{28} + C_{30} + C_{32}} + \frac{C_{25} + C_{27} + C_{29} + C_{31} + C_{33}}{C_{26} + C_{28} + C_{30} + C_{32} + C_{34}}\right) \quad (1)$$

The CPI for *n*-alkanes is a measure of the freshness of terrestrial organic matter. During biosynthesis, higher plants produce odd-numbered long chain *n*-alkanes, but subsequent diagenesis (or a change in the source) leads to homogenization of the distribution (e.g., Eglinton and Hamilton, 1967; Schefuß et al., 2003; Pancost and Boot, 2004). Consequently high CPI values indicate a good preservation of organic matter, whereas low CPI values (~1) suggest its increased degradation (e.g., Schefuß et al., 2003; Jeng, 2006).

The average chain length (ACL) was calculated for *n*-alkanes with the formula (modified from Poynter and Eglinton, 1990):

$$\mathrm{ACL} = \frac{25 \times C_{25} + 27 \times C_{27} + 29 \times C_{29} + 31 \times C_{31} + 33 \times C_{33}}{C_{25} + C_{27} + C_{29} + C_{31} + C_{33}} \quad (2)$$

309 The *n*-C_{35}-alkane was excluded from the formula because of the co-elution with lycopane, a
310 biomarker whose provenance is still under discussion (Sinninghe Damsté et al., 2003;
311 Wakeham et al., 2007). The ACL index is commonly used to monitor changes in long chain
312 *n*-alkane distribution and to identify changes in the sources of higher plant-derived *n*-alkanes
313 (Bush and McInerney, 2015, Diefendorf and Freimuth, 2017; Eley and Hren, 2018).
314
315 **4. Results**
316
317 *4.1. Petrography and mineralogy*
318 The lithological cyclicity of the Pollenzo section is evidenced by the rhythmic
319 repetition of shales and bioturbated marls in cycles Pm3, 4, and 5 and of shales and laminated
320 marls in cycles Pm6 and Pm7 (Fig. 2). These lithological variations are reflected by
321 fluctuations in calcium carbonate contents, with average contents < 20% in the shales, > 40%
322 in the bioturbated marls, and ranging from 20 to 60% in the laminated marls (Table 1, Fig.
323 3A). High calcium carbonate contents were found in the shales of cycle Pm6, due to the
324 presence of aragonite-rich laminae (confirmed by XRD analyses), and in cycle Pg1, due to
325 the presence of dolomite (see below). The bioturbated and laminated marls of each cycles
326 host an indurated carbonate-rich bed (with calcium carbonate contents ranging from 43% to
327 68%). Petrographic features of these beds have been reported in Dela Pierre et al. (2012).
328 The lower part of both the pre-MSC and MSC cycles consists of finely laminated
329 olive to gray shales, representing organic-rich shales with high TOC contents (1.5 - 2%, see
330 below; Fig. 3B). These sediments are irregularly interbedded with cm-thick sandy and silty
331 layers interpreted as the product of high energy fluvial floods (Dela Pierre et al., 2014; Figs.
332 3B, 4C). Lamination is defined by the alternation of sub-mm thick dark terrigenous laminae
333 and whitish laminae (Fig. 4A), which mostly consist of fluorescent peloids (Fig. 4D). Two

types of peloids were recognized: (1) irregular aggregates up to 300 μm across (Fig. 4B), which are composed of silt-sized terrigenous grains, clay, and altered diatom frustules (Fig. 5A), particularly abundant in cycles Pm6 and 7; (2) fecal pellets, up to 0.5 mm across and with an average length of a few mm, characterized by a distinct ovoid or subcyclindrical shape (Figs. 4E, F). These pellets are composed of a mixture of siliciclastic grains and monospecific assemblages of coccoliths, especially in cycles Pm5 and Pm6 (Fig. 5B). The coccoliths are engulfed in amorphous silica, most likely derived from the dissolution of diatoms. Other components are planktic foraminifers (*Orbulina universa, Globigerina bulloides*, *Globigerinita* spp., *Globigerinoides* spp. and *Globoturborotalita apertura* gr.), the abundance of which decrease dramatically in the MSC cycles, where only specimens smaller than 125 μm (*Turborotalita quinqueloba*, *Globigerinita* spp., *Neogloboquadrina* spp.) have been recorded (Fig. 4C; Violanti et al., 2013). Pyrite framboids are abundant (inset Fig. 5C). Their small size, ranging from 3 to 7 μm, suggests a possible origin within the water column (Wilkin et al., 1996).

Gray, strongly bioturbated marls characterize the upper part of cycles Pm3, Pm4, and Pm5 (Fig. 3C). Apart from benthic foraminifers, which are particularly abundant in cycles Pm3 and Pm4, the marls are rich in silt-sized detrital grains, mostly quartz and mica flakes. Planktic foraminifers are scarce (Violanti et al., 2013).

Organic carbon-rich laminated marls (TOC content > 2%, see below) form the upper part of cycles Pm6 and Pm7 and are also found in cycle Pg1 just below the gypsum. The lamination is defined by an alternation of terrigenous-rich gray laminae and whitish laminae (Figs. 3D, E, 5D). The latter are rich in fluorescent curved and straight filaments, up to 70 μm across and several mm long (Figs. 4G, H, I and 5E), which commonly contain micron-sized iron sulfide grains. These filaments, also observed in indurated beds f and g, have been attributed to fossil colorless sulfide-oxidizing bacteria like *Beggiatoa* or *Thioploca* (see Dela

359 Pierre et al., 2012, 2014), and apparently correspond to the filamentous fossils found in
360 Messinian gypsum (Dela Pierre et al., 2015). In cycles Pm7 and Pg1, the filaments are coated
361 by spheroidal dolomite microcrystals with a hollow core (Fig. 5F) of probable microbial
362 origin (cf. Lindtke et al., 2011) and are found in well laminated whitish layers (Fig. 3F). Rare,
363 small sized foraminifers (< 125 μm) and calcareous nannofossils are present up to cycle Pm7
364 (Violanti et al., 2013).
365
366 *4.2. Element and Total Organic Carbon (TOC) fluctuations*
367 The Si/Al, Ti/Al, K/Al, Mg/Al, and Zr/Al ratios display a cyclical trend in phase with
368 lithological cyclicity (Fig. 6; Supplementary Table 1), with lower ratios in shales and higher
369 values in bioturbated marls and especially in the filament-bearing laminated marls of cycles
370 Pm6, Pm7, and Pg1. In cycle Pg1, anomalously high Mg/Al ratios were obtained, which most
371 likely are related to abundant dolomite microcrystals (Figs. 5F, 6). The Ba/Al ratio reveals a
372 cyclic pattern too, but covaries negatively with the Ti/Al, Si/Al, K/Al, Mg/Al, and Zr/Al
373 ratios, being higher in the shales and lower in the bioturbated and laminated marls (Fig. 6).
374 The TOC contents in the pre-MSC deposits (cycles Pm3 and Pm4) follow the
375 lithological cyclicity and are higher in the shales (mean values ~2.0%) than in the bioturbated
376 marls (mean values ~1.4%; Fig. 7). In the MSC deposits, however, highest TOC contents
377 were observed in the laminated marls from cycles Pm6, Pm7 (values > 2%), and especially
378 Pg1 (values up to 3.3%).
379
380 *4.3 Molecular fossils: n-alkane distribution, ratios and stable carbon isotope composition*
381 The *n*-alkane chain lengths vary between C_{15} and C_{37} with the predominance of odd
382 chain lengths from C_{29} to C_{33} *n*-alkanes (Fig. 8). The average chain length (ACL) shows a
383 slight upward decrease from cycle Pm4 (ACL = 29.7) to Pm6 (ACL = 29.1), whereas the

values increase in cycle Pg1 to 29.8 (Fig. 6). Among the short chain *n*-alkanes, the most abundant chains are C_{19} to C_{21} with contents ranging from ~ 1 μg/g TOC in the bioturbated and laminated marls to ~ 12 μg/g TOC (cycle Pm6) in the shales. The long chain (C_{29}-C_{33}) *n*-alkane abundances show the same cyclic fluctuation with minimum contents in the marls (~ 20 μg/g TOC in cycle Pg1) and maximum contents in the shales (up to 236 μg/g TOC in cycle Pm5; see Fig. 7, Table 2 and Supplementary Table 2).

The CPI of *n*-alkanes (CPI) ranges from 2 to 9 (Fig. 7). A negative correlation between the CPI and the *n*-alkane contents is evident, with lower CPI values (~ 2-6) observed in the shales and slightly higher CPI values (up to 9) in the bioturbated and laminated marls.

Table 2
Average molecular fossil abundances (alk = alkane).

	Shales	Bioturbated marls	Laminated marls
∑ *n*-C_{29-33} alk (μg/g TOC)	126.3	68.9	95.3
∑ *n*-C_{19-21} alk (μg/g TOC)	4.6	1.5	2.0
No. of samples	24	9	9

The $\delta^{13}C$ values of long chain *n*-alkanes (C_{29-33}) range from −36‰ to −29‰ (Figs. 7, 9 and Supplementary Table 2). The bioturbated and laminated marls, but especially the carbonate layers are typified by low $\delta^{13}C$ values. A trend towards lower $\delta^{13}C$ values is observed across the onset of the MSC from cycle Pm4 to Pm6. In cycles Pm7 and Pg1, a trend towards higher values is observed. Apart from these trends, the shales are generally characterized by higher $\delta^{13}C$ values, with positive shifts up to ~ 8‰ in comparison with the bioturbated and laminated marls.

4. Discussion

405 *5.1. Fluctuations of element abundances and insights on the provenance of the fine-*
406 *grained detrital fraction*

407 The chemical composition of the Pollenzo sediments provides information on climate
408 by identifying specific sedimentary components that have been transported to the basin by
409 aeolian or fluvial processes during dry and wet climatic periods, respectively (e.g., Wehausen
410 and Brumsack, 2000; Martinez-Ruiz et al., 2000; Calvert and Pedersen, 2007). In particular,
411 Ti/Al, Si/Al, and Zr/Al ratios are used to track aeolian transport. Titanium is enriched
412 compared to Al in soils during phases of intense chemical weathering and is wind transported
413 in the detrital silt-sized fraction as rutile, titanite, and other Ti-rich minerals during arid
414 phases (Moller et al., 2012; Van der Laan et al., 2012). In contrast, the Ti/Al ratio drops
415 during humid phases, when the denser vegetation cover decreases the deflation potential of
416 the surface (e.g., Moller et al., 2012). Silicon and Zr are mostly sourced by quartz and zircon,
417 respectively; these minerals are very resistant to weathering and are enriched in aeolian dust
418 (Schnetger, 1992).

419 In the Pollenzo section, the fluctuations of element abundances display an excellent
420 correlation with the lihological cyclicity in both the pre-MSC and MSC cycles (Fig. 6). The
421 high Ti/Al, Zr/Al, and Si/Al ratios observed in the bioturbated (cycles Pm3, 4 and 5) and
422 filament-bearing laminated marls (cycles Pm6 and Pm7 and Pg1) reflect arid climate and
423 predominant aeolian transport of the detrital fraction. The low element/Al ratios (Figs. 6,
424 10A, B) in the shales on the other hand point to an increase in riverine transport during more
425 humid climatic conditions. Interestingly, in the first gypsum bearing cycle (Pg1), the onset of
426 the arid phase does not coincide with deposition of gypsum, as commonly assumed (e.g.,
427 Krijgsman et al., 2001; Lugli et al 2010; Manzi et al 2013); rather a sharp increase of the
428 Ti/Al ratio is observed approximately 1 meter below the gypsum, coinciding with the
429 appearance of the laminated marls (Fig. 5).

Additional information is provided by K/Al and Mg/Al ratios (Figs. 6, 10C). These ratios reflect the composition of clay minerals transported to the basin (Calvert and Pedersen, 2007). Low K/Al and Mg/Al ratios indicate a predominance of K- and Mg-poor clay minerals such as those of the smectite group. In the northern Adriatic Sea, smectite-rich sediments are currently supplied by the Po River and tributary rivers draining the Alpine and the Apennines catchment areas (Boldrin et al., 1988). Smectite minerals are especially abundant (around 20% of the overall clay minerals) in Mediterranean Pliocene sapropels from the Levantine (e.g., IODP site 967) and the Ionian basins (IODP site 964; Foucault and Mélières, 2000), where they are regarded to be mostly sourced from the Nile river or from rivers of the northern borderland of the eastern Mediterranean (Wehausen and Brumsack, 2000; Hamann et al., 2009; Zhao et al., 2016), respectively. In contrast, high K/Al and Mg/Al ratios indicate a greater contribution of illite (K-rich) and chlorite (Mg-rich), which are common components of aeolian dusts (Tomadin et al., 1984; Tomadin and Lenaz, 1989; Wehausen and Brumsack, 2000; Hamann et al., 2009). However, these ratios alone should only be used with caution, since lower amounts of illite and chlorite can also be supplied by rivers (Tomadin, 2000); in the northern Mediterranean Sea these minerals are supplied by rivers draining the Alpine metamorphic basement (Foucault and Mélières, 2000). Therefore, their use for paleoclimate and provenance reconstructions needs to be validated by other proxies like the Ti/Al ratio and the distribution of terrestrial-sourced molecular fossils (e.g., *n*-alkanes).

In the case of the Pollenzo section, in both the pre-MSC and MSC shales the K/Al and Mg/Al ratios are lower than in the bioturbated and laminated marls (Fig. 10C). Such a pattern is in agreement with the clay mineralogy data, indicating the predominance of smectite (~47%) in the shales of cycle Pm6 (sample Pm6_4.1; Fig. 11) and suggests that the detrital clay fraction was mostly supplied by rivers during more humid phases. Interestingly, the

455 Al_2O_3 contents of the Pollenzo sediments fall between the range of Pleistocene and modern
456 fluvial sediments transported by the Po River, whose main catchment area is the Alpine chain
457 (Amorosi et al., 2002; Fig. 10A). This observation confirms that the detrital material in the
458 Piedmont Basin had a regional origin from the neighboring Alpine domains in agreement
459 with the inferred accelerated denudation of the south-westernmost sector of the Alps between
460 7 and 5 Ma (Foeken et al., 2003; Carrapa and Garcia-Castellanos, 2005; Willet et al., 2006).
461 The K/Al and Mg/Al ratios of bioturbated marls (cycles Pm3-Pm5) and laminated
462 marls of cycle Pm6 are higher than those of shales, confirming – along with the higher Ti/Al
463 and Zr/Al ratios – the prominent role of aeolian transport (Fig. 10A). However, the total Al
464 content of marls is only slightly lower than that of shales, which points to the persistence of
465 riverine input of detrital material even during more arid phases (Figs. 10A, B). The apparent
466 coexistence of aeolian and fluvial transport during dryer conditions is further confirmed by
467 the clay mineral assemblage in the bioturbated marls of cycle Pm6 (sample Pm6_1.1; Fig.
468 11), reflecting similar amounts of riverine smectite and aeolian illite. Interestingly,
469 palygorskite is absent and kaolinite is scarce in marls (6%). Since these minerals are typical
470 components of Saharan dusts (Foucault and Mélières, 2000; Zhao et al., 2016; Ehrmann et
471 al., 2017), an African origin of aeolian material is unlikely for the Pollenzo section. The
472 predominance of illite and chlorite is rather consistent with a northern provenance of aeolian
473 dust. These minerals are abundant in dust sourced from the North today (i.e. the European
474 hinterland), and their contents decrease southward (Tomadin et al., 1984; Tomadin and
475 Lenaz, 1989). A slight change in the ratio of fluvial to aeolian transport is possibly recorded
476 in the laminated marls of cycles Pm7 and Pg1 prior to the first occurrence of gypsum in the
477 Pollenzo section. Although the Mg/Al ratio is compromised by the presence of dolomite, the
478 increased Ti/Al and Zr/Al ratios and the overall decrease of Al contents indicate relatively
479 less riverine input (Figs. 10A, B).

Based on calcareous microfossil assemblages, such oscillations between humid and arid phases have already been described for the pre-MSC cycles of the Pollenzo section (Lozar et al., 2018) and other Mediterranean sections (Sierro et al., 2001, 2003; Kouwenhoven et al., 2006; Gennari et al., 2018). The data presented here reveal that variations in element abundance in the microfossil-poor cycles of the MSC follow the same trends as in the pre-MSC cycles. Our new data provide for the first time independent evidence that lithological cyclicity during the early stage of the MSC was controlled by precession-driven changes in insolation.

5.2 *Precession-controlled variation of sources of organic matter*

5.2.1. Influence of preservation, terrestrial input, and productivity on TOC fluctuations

The TOC content of sediments is a function of the flux of organic carbon from both terrestrial and aquatic sources and preservation, with the latter controlled by the rate of oxidation in the water column and the subseafloor (Calvert and Pederson, 2007; Schoepfer et al., 2015). Aerobic bacterial respiration is the most efficient pathway of organic carbon remineralization (Berner et al., 1984). Oxygen depletion in bottom waters consequently favors the preservation of organic carbon, resulting in high TOC contents even when the flux of organic carbon is low (Van Os et al., 1994; Nijenhuis and de Lange, 2000; Calvert et al., 1992; Rohling et al., 2015). In addition, preservation is favored by high sedimentation rates, decreasing the residence time of sediments at the seafloor and consequently reducing their exposure to oxygen (e.g., Schoepfer et al., 2015). Because the average sedimentation rate, obtained by dividing the thickness of each cycle by its duration (approximatively 20 ka), remained almost constant across the onset of the MSC in the Pollenzo section (15 cm/kyr;

504 Natalicchio et al., 2017), the high TOC contents of the shales must have been caused by other
505 factors.

506 Changes in TOC contents follow lithological cyclicity with higher contents in shales
507 (mean value of 2.0%) than in bioturbated marls (1.4%), although higher contents were
508 observed in the laminated marls of cycles Pm6, Pm7, and especially Pg1 (up to 3.3%). TOC
509 enrichment coincides with evidence of bottom water oxygen depletion, such as lamination,
510 absence of bioturbation and of benthic foraminifers, as well as high pyrite contents. These
511 observations suggest that reducing conditions at the seafloor favored organic carbon
512 preservation. However, the positive covariation of TOC contents with the terrestrial long
513 chain *n*-alkanes and the Ba/Al profile, the latter reflecting primary productivity (see below),
514 suggests that organic carbon accumulation was a function of the combined effects of (1)
515 variations in marine productivity, (2) input of terrestrial organic matter, and (3) enhanced
516 preservation. Overall, the excellent correlation of TOC with lithology and the element-based
517 paleoclimatic proxies (see above) strongly suggests that the supply of organic carbon was
518 controlled by precession as documented for many pre-MSC sequences (cf. Nijenhuis et al.,
519 1996; Schenau et al., 1999; Vazquez et al., 2000; Mayser et al., 2017) and younger Pliocene
520 and Pleistocene sapropelitic sequences (cf. Rohling et al., 2015).

521

522 *5.2.2. The supply of terrestrial organic matter: fluvial versus aeolian transport*

523 Long chain *n*-alkanes are common constituents of the epicuticular waxes of terrestrial
524 higher plants and for this reason are used as proxies of terrestrial organic matter input (e.g.,
525 Eglinton and Hamilton, 1963; Diefendorf et al., 2011). Their water insolubility and resistance
526 to biodegradation makes these molecular fossils excellent recorders of climate-controlled
527 change in terrestrial vegetation and input from the continent (e.g., Schefuß et al., 2003;
528 Pancost and Boot, 2004). In the Pollenzo section, the abundance of long chain *n*-alkanes

increases in the upper part of the section, with maximum contents in the MSC cycles (Pm6-Pm7; Fig. 7; Table 1). This trend reflects an increased input of terrestrial organic matter during the first phase of the MSC. Long-chain *n*-alkanes reveal a cyclic pattern and a negative covariation with element/Al ratios, but a positive correlation with the total Al content. Taken together, these observations suggest that wet phases (low Ti/Al ratio) during insolation maxima – represented by shales – were characterized by maximum influx of terrestrial organic matter mainly supplied by rivers. Such covariation is particularly pronounced in the MSC part of the section (e.g., cycle Pm6; Fig. 6). During arid phases (high Ti/Al ratio) at times of insolation minima – represented by bioturbated and laminated marls – influx of terrestrial organic matter from rivers was reduced due to the advent of more arid condition dominated by aeolian transport, which supplied a limited amount of organic matter.

5.2.3. Climate controlled variations of the source of terrestrial organic matter

The average chain length (ACL) of *n*-alkanes, the $n\text{-}C_{31}/(n\text{-}C_{29}+n\text{-}C_{31})$, and the compound-specific carbon isotope compositions of *n*-alkanes can be used to reconstruct the type of vegetation from which they were produced (e.g., Eglinton and Hamilton, 1963; Pancost and Boot, 2004; Diefendorf and Freimuth, 2017). Fluctuations among these proxies can be caused by changing contributions of plant species with different photosynthetic pathways (C_3 and C_4) to the pool of terrestrial organic matter (Castaneda et al., 2007), which is controlled by climate. It has been demonstrated that C_3 plants, which use the Calvin-Benson cycle and prefer colder and more humid climate, tend to produce shorter *n*-alkane chains, resulting in low ACL and $n\text{-}C_{31}/(n\text{-}C_{29}+n\text{-}C_{31})$ ratios (e.g., Rommerskirchen et al., 2006; Shepherd and Griffiths, 2006; Bush and McInerney, 2013, 2015), than C_4 plants. The latter use the Hatch-Slack cycle and are better adapted to more arid and warmer conditions (e.g., Schefuß et al., 2003; Ortiz et al., 2013). In addition, the compound specific carbon

554 isotopes ($\delta^{13}C$) of *n*-alkanes produced by C_3 plant waxes generally show more negative $\delta^{13}C$
555 values (−38‰ to −32‰) than those of C_4 plants (−25‰ to −18‰; Collister et al., 1994;
556 Naafs et al., 2012). In the Pollenzo section the slight decrease of the ACL, of the $n\text{-}C_{31}/(n\text{-}C_{29}+n\text{-}C_{31})$ ratio and of the $\delta^{13}C$ values (~ 4‰ for C_{29} and ~ 7‰ for $C_{31\text{-}33}$) across the MSC
558 onset (up to cycle Pm6) is negatively correlated with the progressive increase of content of
559 terrestrial organic matter (Fig. 7). These trends are consistent with C_3-dominated vegetation,
560 possibly reflecting an increase of humidity during the first phases of the MSC. In contrast, the
561 increase of the *n*-alkane ratios (ACL and $n\text{-}C_{31}/(n\text{-}C_{29}+n\text{-}C_{31})$) and the ^{13}C enrichment ($\delta^{13}C$
562 shift ~ +4‰) observed from cycle Pm7 upward suggests the establishment of dryer
563 conditions (e.g., Eley and Hren, 2018) responsible for a vegetation change. This change is
564 reflected by higher proportions of C_3 plants adapted to more arid conditions and/or an
565 increased contribution of arid-prone C_4 plants (e.g., Diefendorf et al., 2011; Mayser et al.,
566 2017).

567 The closer inspection of the *n*-alkanes ratios and isotopic composition at the scale of
568 the single lithological cycles reveals that shales yields values at the higher end (Figs. 7, 9),
569 which is surprising. These values suggest greater contributions of C_4 plants (or of ^{13}C-
570 enriched C3 plants), in contrast to the notion that shales were formed during more humid
571 periods. This inconsistency can be explained considering the CPI index, which reflects the
572 state of degradation and source of terrestrial organic matter (e.g., Bray and Evans, 1961;
573 Schefuß et al., 2003). In general, the high CPI values observed for the majority of samples
574 (~5 to 9) indicate good preservation and freshness of terrestrial organic matter supplied by
575 higher plants (Jeng et al., 2006). Nevertheless, CPI shows significant fluctuation with lower
576 values in the shales (as low as 2-3) and higher values in the bioturbated and laminated marls
577 (as high as 8-9). Being out of phase with the *n*-alkane profile (Fig. 7), the lower CPI values of
578 shales possibly reflect enhanced contribution of altered, mature terrestrial organic matter,

579 recycled from older sediments (cf. Cortina et al., 2016). Therefore, the paleoclimate
580 reconstructions based on *n*-alkane ratios and compound specific $\delta^{13}C$ values from shales (Fig.
581 9) may be seriously biased. Such bias is apparently not affecting the bioturbated and
582 laminated marls with their higher CPI values, reflecting fresher terrestrial organic matter
583 mostly sourced from coeval plants growing close to the basin margins (Cortina et al., 2016).
584
585 *5.2.4. Marine primary productivity: the Ba/Al profile*
586 The Ba content of sediments is used as an indicator of marine primary productivity
587 based on the excellent correlation of organic carbon and Ba in sediments of modern oceans
588 (e.g., Cardinal et al., 2005; Paytan and Griffith, 2007). Barium is closely associated with
589 organic material during settling and is subsequently delivered as barite ($BaSO_4$) to the
590 seafloor (Calvert and Pedersen, 2007; Schoepfer et al., 2015). In the Pollenzo section, the
591 Ba/Al profile shows a cyclic pattern (Fig. 6), revealing a negative covariation with the
592 abundance of major elements (e.g., Si, K, Mg; see above) and a positive correlation with the
593 TOC and the content of terrestrial lipids (with remarkable exceptions for the filament-bearing
594 laminated marls of cycles Pm6, Pm 7 and Pg1; see below). These patterns indicate that
595 marine primary productivity was increased during the deposition of the smectite-rich shales at
596 times of insolation maxima, associated with the increased input of terrestrial lipids by
597 enhanced riverine runoff. Probably, enhanced riverine runoff was responsible for an
598 increased nutrient input into the basin, which caused eutrophication of the upper water
599 column (cf. Friedrich et al., 2014). The facts that (1) shales contain abundant fecal pellets and
600 clay rich aggregates with altered diatom frustules – both common components of marine
601 "snow" forming in the upper oxygenated layers during episodes of enhanced productivity
602 (Alldredge and Silver, 1988; Dela Pierre et al., 2014) – and (2) planktic foraminifer

603 assemblages with abundant eutrophic taxa typify pre-MSC cycles (Lozar et al., 2018) agree
604 with such an interpretation.
605 The Ba profile could have been altered by post-depositional loss of accumulated barite
606 in anoxic sediments. Barite tends to dissolve when exposed to anoxic pore waters from which
607 sulfate is removed by intense bacterial sulfate reduction (e.g., Schoepfer et al., 2015).
608 Oxygen-depleted bottom conditions during the deposition of the shales are suggested by the
609 fine lamination of sediments and the absence of bioturbation. In addition, high contents of
610 pyrite framboids agree with formerly pronounced bacterial sulfate reduction in the studied
611 sediments. However, the Gaussian-shaped Ba/Al profile and the symmetrical Ba peaks
612 strongly suggest that Ba distribution reflects changes in paleoproductivity (cf. Wehausen and
613 Brumsack, 1999). Sulfate reduction was apparently not sufficient to decrease pore water
614 sulfate concentration to the extent necessary for barite dissolution, possibly because sulfate
615 was continuously replenished by seawater (e.g., Martinez Ruiz et al., 2000). This
616 interpretation agrees with the continuous occurrence of marine fossils (foraminifers,
617 calcareous plankton, diatoms, fishes; Sturani, 1973; Violanti et al., 2013; Lozar et al., 2018),
618 indicating a connection of the marginal basin to an open marine water body (Dela Pierre et
619 al., 2014, 2015; Natalicchio et al., 2014), allowing for the supply of dissolved sulfate required
620 for barite preservation.
621 Interestingly, no positive correlation exists between the Ba/Al ratio and the TOC
622 contents in the filament bearing marls of cycles Pm6, Pm7, and Pg1. In these sediments, the
623 high TOC contents (as high as 3%) are not associated with a parallel increase of the Ba/Al
624 ratio, whereas the terrestrial lipid abundance remains constant or even decreases in cycle Pg1.
625 This observation implies that these high TOC contents reflect a source of organic carbon
626 other than terrestrial organic matter or marine primary productivity in the euphotic zone. A
627 possible source includes a contribution from chemoautotrophy, which may agree with the

628 sharp increase of archaeal communities above the MSC onset (Natalicchio et al., 2017) and
629 with the interpretation of the super-abundant filamentous fossils as chemotrophic sulfide-
630 oxidizing bacteria (Dela Pierre et al., 2012; 2014). In modern settings, mats of these bacteria
631 are characterized by high rates of organic carbon accumulation from chemoautotrophy,
632 adding to primary production by photoautotrophy in surface waters (Taylor et al., 2001;
633 Jessen et al., 2016).
634
635 *5.3 Sedimentary response to astronomical forcing across the onset of the MSC*
636 The Messinian organic-rich shales of the Pollenzo section show striking geochemical
637 similarities with the more extensively studied Mediterranean Pliocene and Pleistocene
638 sapropels (cf. Emeis et al., 2000; Rohling et al., 2015), suggesting that a single mechanism –
639 enhanced riverine runoff with an increased supply of terrestrial organic matter and nutrients
640 during insolation maxima – led to increased productivity in the Mediterranean during the late
641 Neogene (e.g., Nijhenhuis et al., 1996; Negri et al., 1999; Schenau et al., 1999). Increased
642 runoff resulted in water column stratification and bottom anoxia, which enhanced
643 preservation of organic carbon (Fig. 12A). However, unlike the Mediterranean sapropels, the
644 source of freshwater in the study area was not the Nile but rivers draining the uplifting Alpine
645 chain. Our data support the notion that during the Late Miocene the Piedmont-Basin was
646 influenced by precessional-driven changes in the intensity of the North Atlantic Storm track
647 (Kutzbach et al., 2014) and/or net convective precipitations over the Mediterranean Sea
648 (Bosmans et al., 2015). Climate simulations suggest that both these mechanisms are able to
649 supply an extra freshwater budget to the Northern Mediterranean at insolation maxima, in
650 phase with the African monsoon (Meijer and Tuenter, 2007; Toucanne et al., 2015).
651 Although the organic-rich shales show similar geochemical and sedimentological
652 patterns throughout most of the Pollenzo section, a change is observed across the MSC onset

653 in the sediments reflecting the arid part of the precessional cycle. Bioturbated marls with low
654 contents of TOC, terrestrial lipids, and Ba occur before the MSC onset (cycles Pm3 and Pm4)
655 and in the earliest part of the MSC (cycle Pm5). In contrast, laminated and filament-bearing
656 marls with high TOC contents (but low Ba contents) are observed in the two cycles above the
657 MSC onset (Pm6 and Pm7) and in cycle Pg1, just below the first gypsum bed. This change
658 possibly reflects variations in bottom water redox conditions, which may have been triggered
659 by changes in the climatic or physiographic conditions of the basin after the onset of the MSC
660 at times of insolation minima (Fig. 12B). Intense bioturbation of marls points to oxygenated
661 bottom water conditions, which are best explained by low freshwater inflow in accordance
662 with the reduced input of terrestrial lipids and decreased productivity as indicated by low Ba
663 contents. These conditions favored mixing of the water column and flow of oxygen-rich
664 waters to greater depth (e.g., Sierro et al., 2003; Friedrich et al., 2014). High bottom water
665 oxygenation correspondingly lowered the preservation potential of organic carbon, which
666 together with the reduced primary productivity and reduced supply of terrestrial organic
667 matter resulted in low TOC contents.

668 In contrast, the massive occurrence of filamentous microfossils assigned to colorless
669 sulfide-oxidizing bacteria in the laminated marls (Dela Pierre et al., 2012, 2014, 2015) is in
670 accord with hypoxic bottom waters after the MSC onset (Fig. 12C). A comparison with
671 modern settings indicates that these bacteria form dense microbial mats on the seafloor under
672 variable hypoxic conditions (Schultz and Jørgensen, 2001; Mussmann et al., 2003). Growth
673 of chemotrophic sulfide-oxidizing bacteria is particularly favored by steep gradients of
674 molecular oxygen or dissolved nitrate and hydrogen sulfide. Such conditions occur when the
675 chemocline, separating oxygenated from anoxic waters below, impinges the sea bottom
676 (Jessen et al., 2016). Likewise, water column stratification may even have occurred during
677 insolation minima after the MSC onset, which is supported by the presence of tetrahymanol

678 in the laminated marls (Natalicchio et al., 2017). This compound is found in bacterivorous
679 ciliates (e.g., *Tetrahymena pyriformis*; Harvey and McManus, 1991), anoxygenic
680 phototrophic bacteria (e.g., Eickhoff et al., 2013), and aerobic methanotrophic bacteria (Banta
681 et al., 2015), all of which are abundant at chemoclines. Tetrahymanol (or its degradation
682 product gammacerane) is consequently considered to be indicative of water-column
683 stratification (Sinninghe Damsté et al., 1995).

684 In a marginal basin with limited water exchange with the global ocean, such as the
685 Piedmont Basin during the Messinian (Sturani, 1973; Dela Pierre et al., 2011), intensification
686 of water column stratification can result from steep thermal and salinity gradients, which are
687 induced by warming of the upper water column or increased freshwater inflow from
688 precipitation or riverine runoff (e.g., Friedrich et al., 2014). Warming is not indicated by
689 current paleoclimate reconstructions, which rather suggest a cooling trend during the late
690 Neogene (Herbert et al. 2016). Increased freshwater input is indicated by rising contents of
691 terrestrial molecular fossils from the pre-MSC bioturbated marls to the MSC filament-bearing
692 laminated marls of cycle Pm6. The shift toward more ^{13}C-depleted long chain *n*-alkanes and
693 the shortening of their chain lengths suggests that a C_3-dominated terrestrial vegetation
694 adapted to humid climate existed at that time. Paleobotanical data revealed strong climate
695 gradients within the Mediterranean during the MSC, with the northern sub-basins (e.g.,
696 Piedmont and Vena del Gesso) characterized by moist climate and a positive hydrological
697 budget (Bertini and Martinetto, 2011), in line with the findings of this study.
698

699 **6. Conclusions**

700

701 Trends in major and trace elements as well as molecular fossils allow assessing of the
702 relationship between sedimentary cyclicity and precessional forcing in Messinian fossil-poor

703 strata from the Piedmont Basin. In the studied Pollenzo section, organic-rich shales, which
704 deposited during insolation maxima, remained unchanged across the onset of the MSC with
705 respect to their geochemical and sedimentological characteristics. The higher organic carbon
706 contents of shales compared to other lithologies resulted from increased primary productivity,
707 interpreted to have been triggered by enhanced riverine runoff carrying nutrients into the
708 basin. Moreover, preservation of organic carbon at times of shale deposition was favored by
709 bottom anoxia caused by water column stratification. The mode of formation of the
710 Messinian organic-rich shales was apparently analogous to that inferred for their younger and
711 more extensively studied Pliocene and Pleistocene counterparts (i.e., the Mediterranean
712 sapropels), suggesting that similar mechanisms were responsible for the deposition of
713 organic-rich sediments in the Mediterranean during the Neogene. Conversely, bioturbated
714 and laminated marls deposited during dryer periods at insolation minima before and after the
715 onset of the MSC. The trend from fully oxygenated conditions during marl deposition in pre-
716 MSC times (bioturbated marls) to hypoxic conditions in the earliest MSC phases (laminated
717 marls) is interpreted to reflect increasingly reducing bottom waters. Molecular fossil and
718 element geochemical data suggest that water column stratification was intensified by the
719 combined effects of persistent freshwater input and basin restriction heralding gypsum
720 precipitation in this relatively deep basin. The used multi-proxy approach, combining
721 sedimentological and petrographical analyses with element geochemistry and molecular
722 fossils, has great potential for the reconstruction of climate-induced environmental change in
723 sediments that are devoid of fossils. It may help to decipher the causes of severe
724 environmental crises in Earth history.
725
726
727 **Acknowledgments**

728 We thank P. Clari (University of Torino) for his continuous support and discussions, S.
729 Cavagna (University of Torino) for help with SEM/EDS analyses, S. Beckmann (University
730 of Hamburg) for precious technical support in the organic geochemistry laboratory, D.
731 Bortels (University of Hamburg) for help with extraction of lipid biomarkers, R. Lendt
732 (University of Hamburg) for measurement of $\delta^{13}C$ isotope values of *n*-alkanes, J. Richarz
733 (University of Hamburg) for the analysis of TOC and $CaCO_3$ contents, and E. Vinx
734 (University of Hamburg) for thin sections preparation. This project has received funding from
735 the European Union's Horizon 2020 research and innovation program under the Marie
736 Skłodowska-Curie grant agreement No. 658252 and from University of Torino (ex 60%
737 grants in 2015 and 2016 to FD). The article is further based upon work from COST Action
738 "Uncovering the Mediterranean salt giant" (MEDSALT) supported by COST (European
739 Cooperation in Science and Technology). Insightful comments by two anonymous reviewers
740 helped improve the manuscript.
741
742
743 **References**
744 Algeo, T.J., Tribovillard, N., 2009. Environmental analysis of paleoceanographic systems
745 based on molybdenum-uranium covariation. Chemical Geology 268, 211–225.
746 Alldredge, A.L., Silver, M.W., 1988. Direct observations of the mass flocculation of diatom
747 blooms: characteristics, settling velocities, and formation of diatom aggregates.
748 Limnology and Oceanography 20, 41–82.
749 Amorosi, A., Centineo, M.C., Dinelli, E., Lucchini, F., Tateo, F., 2002. Geochemical and
750 mineralogical variations as indicators of provenance changes in Late Quaternary
751 deposits of SE Po Plain. Sedimentary Geology 151, 273–292.

752 Bąbel, M., 2007. Depositional environments of a salina type evaporite basin recorded in the
753 Badenian gypsum facies in northern Carpathian Foredeep, In: Schreiber, B. C., Lugli,
754 S., Bąbel, M. (Eds), Evaporites Through Space and Time. Geological Society of
755 London, Special Publication 285, 107–142.
756 Banta, A.B., Wie, J.H., Welander, P.V., 2015. A distinct pathway for tetrahymanol synthesis
757 in bacteria. Proceedings of the National Academic of Sciences USA 112, 13478–
758 13483.
759 Bellanca, A., Caruso, A., Ferruzza, G., Neri, R., Rouchy, J.M., Sprovieri, M., Blanc-Valleron,
760 M. M., 2001. Transition from marine to hypersaline conditions in the Messinian
761 Tripoli Formation from the marginal areas of the central Sicilian Basin. Sedimentary
762 Geology 140, 87–105
763 Berner, R.A., 1984. Sedimentary pyrite formation: an update. Geochimica et Cosmochimica
764 Acta 48, 605–615.
765 Bertini, A., Martinetto, E., 2011. Reconstruction of vegetation transects for the Messinian-
766 Piacenzian of Italy by means of comparative analysis of pollen, leaf and carpological
767 records. Palaeogeography, Palaeoclimatology, Palaeoecology 304, 230–246.
768 Bigi, G., Cosentino, D., Parotto,M., Sartori, R., Scandone, P., 1990. Structural Model of Italy:
769 Geodinamic Project: Consiglio Nazionale delle Ricerche, S.EL.CA, scale 1:500,000,
770 sheet 1.
771 Birgel, D., Thiel, V., Hinrichs, K.-U., Elvert, M., Campbell, K.A., Reitner, J., Farmer J.D.,
772 Peckmann, J., 2006. Lipid biomarker patterns of methane-seep microbialites from the
773 Mesozoic convergent margin of California. Organic Geochemistry 37, 1289–1302.
774 Boldrin, A., Bortoluzzi, G., Frascari, F., Guerzoni, S., Rabitti, S., 1988. Recent deposits and
775 suspended sediments off the Po della Pila (Po River, main mouth), Italy. Marine
776 Geology 79, 159–170.

777 Bosmans, J.H.C., Drijfhout, S.S., Tuenter, E., Hilgen, F.J., Lourens, L.J., Rohling, E.J., 2015.
778 Precession and obliquity forcing of the freshwater budget over the Mediterranean.
779 Quaternary Science Reviews 123, 16–30.
780 Bray, E.E., Evans, E.D., 1961. Distribution of normal-paraffins as a clue to recognition of
781 source beds. Geochimica et Cosmochimica Acta 22, 2–15.
782 Brumsack, H.J, 2006. The trace metal content of recent organic carbon-rich sediments:
783 implications for Cretaceous black shale formation. Palaeogeography,
784 Palaeoclimatology, Palaeoecology 232, 344–361.
785 Bush, R.T., McInerney, F.A., 2013. Leaf wax *n*-alkane distributions in and across modern
786 plants: implications for paleoecology and chemotaxonomy. Geochimica et
787 Cosmochimica Acta 117, 161–179.
788 Bush, R.T., McInerney, F.A., 2015. Influence of temperature and C_4 abundance on *n*-alkane
789 chain length distributions across the central USA. Organic Geochemistry, 79, 65–73.
790 Calvert, S.E., Pedersen, T.F., 2007. Elemental proxies for palaeoclimatic and
791 palaeoceanographic variability in marine sediments: interpretation and application. In:
792 Hillaire- Marcel, C., De Vernal, A. (Eds.), Proxies in Late Cenozoic
793 Paleoceanography, Developments in Marine Geology, vol. 1. Elsevier, 567–644.
794 Capella, W., Matenco, L., Dmitrieva, E., Roest, W.M.J., Hessels, S., Hssain, M., Chakor-
795 Alami, A., Sierro, F.J., Krijgsman, W., 2016. Thick-skinned tectonics closing the
796 Rifian Corridor. Tectonophysics 710-711, 249–265.
797 Cardinal, D., Savoye, N., Trull, T.W., André, L., Kopczynska, E.E., Dehairs, F., 2005.
798 Variations of carbon remineralisation in the Southern Ocean illustrated by the Ba_{xs}
799 proxy. Deep-Sea Research I 52, 355–370.

800 Carrapa, B., Garcia-Castellanos, D., 2005. Western Alpine back-thrusting as subsidence
801 mechanism in the Tertiary Piedmont Basin (western Po Plain, NW
802 Italy). Tectonophysics 406, 197–212.
803 Castaneda, I.S., Werne, J.P., Johnson, T.C., 2007. Wet and arid phases in the southeast
804 African tropics since the Last Glacial Maximum. Geology 35, 823–826.
805 Cita, M.B., Wright, R.C., Ryan, W.B.F., Longinelli, A., 1978. Messinian paleoenvironments,
806 In: Hsü, K.J., Montadert, L. et al. (Eds.), Initial Reports of the Deep Sea Drilling
807 Project 42. U.S. Government Printing Office, Washington D.C, 1003–1035.
808 Collister, J.W., Lichtfouse, E., Hieshima, G., Hayes, J.M., 1994. Partial resolution of sources
809 of *n*-alkanes in the saline portion of the Parachute Creek Member, Green River
810 Formation (Piceance Creek Basin, Colorado). Organic Geochemistry 21, 645–659.
811 Cortina, A., Grimalt, J.O., Rigual-Hernandez, A., Ballegeer, A.M., Martrat, B., Sierro, F.J.,
812 Flores J.A., 2016. The impact of ice-sheet dynamics in western Mediterranean
813 environmental conditions during terminations: an approach based on terrestrial long
814 chain *n*-alkanes deposited in the upper slope of the Gulf of Lions. Chemical Geology
815 430, 21–33.
816 De Lange, G. J., Krijgsman, W., 2010. Messinian salinity crisis: a novel unifying shallow
817 gypsum/deep dolomite formation mechanism. Marine Geology 275, 273–277.
818 Dela Pierre, F., Bernardi, E., Cavagna, S., Clari, P., Gennari, R., Irace, A., Lozar, F., Lugli,
819 S., Manzi, V., Natalicchio, M., Roveri, M., Violanti, D., 2011. The record of the
820 Messinian salinity crisis in the Tertiary Piedmont Basin (NW Italy): The Alba section
821 revisited. Palaeogeography, Palaeoclimatology, Palaeoecology 310, 238–255.
822 Dela Pierre, F., Clari, P., Bernardi, E., Natalicchio, M., Costa, E., Cavagna, S., Lozar, F.,
823 Lugli, S., Manzi, V., Roveri, M., Violanti, D., 2012. Messinian carbonate-rich beds of
824 the Tertiary Piedmont Basin (NW Italy): Microbially-mediated products straddling

the onset of the salinity crisis. Palaeogeography, Palaeoclimatology, Palaeoecology 344–345, 78–93.

Dela Pierre, F., Clari, P., Natalicchio, M., Ferrando, S., Giustetto, R., Lozar, F., Lugli, S., Manzi, V., Roveri, M., Violanti, D., 2014. Flocculent layers and bacterial mats in the mudstone interbeds of the Primary Lower Gypsum unit (Tertiary Piedmont basin, NW Italy): Archives of palaeoenvironmental changes during the Messinian salinity crisis. Marine Geology 355, 71–87.

Dela Pierre, F., Natalicchio, M., Ferrando, S., Giustetto, R., Birgel, D., Carnevale, G., Gier, S., Lozar, F., Marabello, D., Peckmann, J., 2015. Are the large filamentous microfossils preserved in Messinian gypsum colorless sulfide-oxidizing bacteria? Geology 43, 855–858.

Diefendorf, A.F., Freimuth, E.J., 2017. Extracting the most from terrestrial plant-derived *n*-alkyl lipids and their carbon isotopes from the sedimentary record: A review. Organic Geochemistry 103, 1–22.

Diefendorf, A. F., Freeman, K. H., Wing, S. L., Graham, H. V., 2011. Production of *n*-alkyl lipids in living plants and implications for the geologic past. Geochimica et Cosmochimica Acta 75, 7472–7485.

Duggen, S., Hoernie, K., van de Bogaard, P., Rupke, L., Phipps Morgan, J., 2003. Deep roots of the Messinian salinity crisis. Nature 422, 602–606.

Edwards, E.J., Osborne, C.P., Stromberg, C.A., Smith, S.A., Consortium, C.G., 2010. The origins of C_4 grasslands: integrating evolutionary and ecosystem science. Science 328, 587–591.

Eglinton, G., Hamilton, R.J., 1963. The distribution of alkanes. In: Swain T. (Ed.), Chemical plant taxonomy, Academic Press, London, 187–217.

Eglinton, G., Hamilton, R.J., 1967. Leaf epicuticular waxes. Science 156, 1322–1335.

Ehrmann, W., Schmiedl, G., Beuscher, S., Krüger, S., 2017. Intensity of African humid periods estimated from Saharan dust fluxes. PLOS ONE 12, e0170989, doi:10.1371/journal.pone.0170989.

Eickhoff, M., Birgel, D., Talbot, H.M., Peckmann, J., Kappler, A., 2013. Oxidation of Fe(II) leads to increased C-2 methylation of pentacyclic triterpenoids in the anoxygenic phototrophic bacterium *Rhodopseudomonas palustris* strain TIE-1. Geobiology 11, 268–278.

Eley, Y. L., Hren, M. T., 2018. Reconstructing vapor pressure deficit from leaf wax lipid molecular distributions. Scientific Reports 81, 3967.

Emeis, K.C., Sakamoto, T., Wehausen, R., Brumsack, H.J., 2000. The sapropel record of the eastern Mediterranean Sea—results of Ocean Drilling Program Leg 160. Palaeogeography, Palaeoclimatology, Palaeoecology 158, 371–395.

Flecker, R., Krijgsman, W., Capella, W., de Castro Martíns, C., Dmitrieva, E., Mayser, J.P., Marzocchi, A., Modestou, S., Ochoa, D., Simon, D., Tulbure, M., van den Berg, B., van der Schee, M., de Lange, G., Ellam, R., Govers, R., Gutjahr, M., Hilgen, F., Kouwenhoven, T., Lofi, J., Meijer, P., Sierro, F.J., Bachiri, N., Barhoun, N., Alami, A.C., Chacon, B., Flores, J.A., Gregory, J., Howard, J., Lunt, D., Ochoa, M., Pancost, R., Vincent, S., Yousfi, M.Z., 2015. Evolution of the Late Miocene Mediterranean–Atlantic gateways and their impact on regional and global environmental change. Earth-Science Reviews 150, 365–392.

Foeken, J.P.T., Dunai, T.J., Bertotti, G., Andriessen, P.A.M., 2003. Late Miocene to present exhumation in the Ligurian Alps (southwest Alps) with evidence for accelerated denudation during the Messinian salinity crisis. Geology 31, 707–800.

873 Foucault, A., Mélières, F., 2000. Palaeoclimatic cyclicity in central Mediterranean Pliocene
874 sediments: the mineralogical signal. Palaeogeography, Palaeoclimatology,
875 Palaeoecology 158, 311–323.
876 Friedrich, J., Janssen, F., Aleynik, D., Bange, H.W., Boltacheva, N., Çagatay, M.N., Dale,
877 A.W., Etiope, G., Erdem, Z., Geraga, M., Gilli, A., Gomoiu, M.T., Hall P.O.J.,
878 Hansson, D., He, Y., Holtappels, M., Kirf, M.K., Kononets, M., Konovalov, S.,
879 Lichtschlag, A., Livingstone, D.M., , Marinaro, G., Mazlumyan S., Naeher, S. , North,
880 R.P., Papatheodorou, G., Pfannkuche, O., Prien, R., Rehder, G., Schubert, C.J.,
881 Soltwedel, T., Sommer, S., Stahl, H., Stanev, E.V, Teaca, A., Tengberg, A.,
882 Waldmann, C., Wehrli, B., Wenzhöfer, F., 2014. Investigating hypoxia in aquatic
883 environments: diverse approaches to addressing a complex phenomenon.
884 Biogeosciences 11, 1215–1259.
885 Garcia-Castellanos, D., Villaseñor, A., 2011. Messinian salinity crisis regulated by competing
886 tectonics and erosion at the Gibraltar arc. Nature 480, 359–363.
887 Gennari, R., Manzi, V., Angeletti, L., Bertini, A., Biffi, U., Ceregato, A., Faranda, C.,
888 Gliozzi, E., Lugli, S., Menichetti, E., Rosso, A., Roveri, M., Taviani, M., 2013. A
889 shallow water record of the onset of the Messinian salinity crisis in the Adriatic
890 foredeep (Legnagnone section, Northern Apennines). Palaeogeography,
891 Palaeoclimatology, Palaeoecology 386, 145–164.
892 Gennari, R., Lozar, F., Turco, E., Dela Pierre, F., Manzi, V., Natalicchio, M., Lugli, S.,
893 Roveri, M., Schreiber, B.C., Taviani, M., 2018. Integrated stratigraphy and
894 paleoceanographic evolution of the pre-evaporitic phase of the Messinian salinity
895 crisis in the Eastern Mediterranean as recorded in the Tokhni section (Cyprus island).
896 Newsletters on Stratigraphy 51/1, 33–55.

Gladstone, R., Flecker, R., Valdes, P., Lunt, D., Markwick, P., 2007. The Mediterranean hydrologic budget from a Late Miocene global climate simulation. Palaeogeography, Palaeoclimatology, Palaeoecology 251, 254–267.

Hamann, Y., Ehrmann, W., Schmiedl, G., Kuhnt, T., 2009. Modern and late Quaternary clay mineral distribution in the area of the SE Mediterranean Sea. Quaternary Research 71, 453–464.

Harvey, H.R., McManus, G.B., 1991. Marine ciliates as a widespread source of tetrahymanol and hopan-3β-ol in sediments. Geochimica et Cosmochimica Acta 55, 3387–3390.

Herbert, T.D., Lawrence, K.T., Tzanova, A., Peterson, L.C., Caballero-Gill, R., Kelly, C.S., 2016. Late Miocene global cooling and the rise of modern ecosystems. Nature Geosciences 9, 843–847.

Hilgen, F.J., Krijgsman, W., 1999. Cyclostratigraphy and astrochronology of the Tripoli diatomite formation (pre-evaporite Messinian, Sicily, Italy). Terra Nova 11, 16–22.

Hilgen, F., Kuiper, K., Krijgsman,W., Snel, E., van der Laan, E., 2007. Astronomical tuning as the basis for high resolution chronostratigraphy: the intricate history of the Messinian Salinity Crisis. Stratigraphy 4, 231–238.

Hsü, K., Montadert, L., Bernoulli, D., Cita, M.B., Erickson, A., Garrison, R.E., Kidd R.B., Mèlierés, F., Müller, C., Wright, R., 1977. History of the Mediterranean salinity crisis. Nature 267, 399–403.

Irace, A., Dela Pierre, F., Clari, P., 2005. “Normal” and “chaotic” deposits in the Messinian Gessoso-solfifera Fm. at the north eastern border of the Langhe domain (Tertiary Piedmont basin). Bollettino Società Geologica Italiana 4, 77–85.

Irace, A., Clemente, P., Natalicchio, M., Ossella, L., Trenkwalder, S., De Luca, D. A., Mosca, P., Piana, F., Polino, R., Violanti, D., 2010. Geologia e idrostratigrafia profonda della

921 Pianura Padana occidentale: La Nuova Lito Firenze, pp. 110, ISBN 978-88-904554-0-
922 7.
923 Jeng, W.L., 2006. Higher plant *n*-alkane average chain length as an indicator of petrogenic
924 hydrocarbon contamination in marine sediments. Marine Chemistry 102, 242–251.
925 Jessen, G.L., Lichtschlag, A., Struck, U., Boetius, A., Reese, B.K., Texas, A., Christi, M.U.,
926 2016. Distribution and composition of thiotrophic mats in the hypoxic zone of the
927 Black Sea (150–170 m water depth, Crimea margin). Frontiers in Microbiology 7, 1–
928 14.
929 Krijgsman, W., Hilgen, F., Raffi, I., Sierro, F., Wilson, D., 1999. Chronology, causes and
930 progression of the Messinian salinity crisis. Nature 400, 652–655.
931 Krijgsman, W., Fortuin, A.R., Hilgen, F.J., Roep, T.B., Sierro, F. J., 2001. Astrochronology
932 for the Messinian Sorbas Basin (SE Spain) and orbital (precessional) forcing for
933 evaporite cyclicity. Sedimentary Geology 140, 43–60.
934 Kouwenhoven, T.J., Morigi, C., Negri, A., Giunta, S., Krijgsman, W., Rouchy, J.M., 2006.
935 Palaeoenvironmental evolution of the eastern Mediterranean during the Messinian:
936 constraints from integrated microfossil data of the Pissouri Basin (Cyprus). Marine
937 Micropalaeontology 60, 17–44.
938 Kutzbach, J.E., Chen, G., Cheng, H., Edwards, R.L., Liu, Z., 2014. Potential role of winter
939 rainfall in explaining increased moisture in the Mediterranean and Middle East during
940 periods of maximum orbitally-forced insolation seasonality. Climate Dynamics 42,
941 1079 –1095.
942 Laskar, J., Robutel, P., Joutel, F., Gastineau, M., Correia, A.C.M., Levrard, B., 2004. A long-
943 term numerical solution for the insolation quantities of the Earth. Astronomy and
944 Astrophysics 428, 261–285.

945 Lindtke, J., Ziegenbalg, S.B., Brunner, B., Rouchy, J.M., Pierre, C., Peckmann, J. 2011.
946 Authigenesis of native sulphur and dolomite in a lacustrine evaporitic setting (Hellín
947 basin, Late Miocene, SE Spain). Geological Magazine 148, 655–669.
948 Lozar, F., Violanti, D., Dela Pierre, F., Bernardi, E., Cavagna, S., Clari, P., Irace, A.,
949 Martinetto, E., Trenkwalder, S., 2010. Calcareous nannofossils and foraminifers
950 herald the Messinian Salinity Crisis: The Pollenzo section (Alba, Cuneo; NW Italy).
951 Geobios 43, 21–32.
952 Lozar, F., Violanti, D., Bernardi, E., Dela Pierre, F., Natalicchio, M. 2018. Identifying the
953 onset of the Messinian salinity crisis: a reassessment of the biochronostratigraphic
954 tools (Piedmont Basin, NW Italy). Newsletter on Stratigraphy 51/1, 11–31.
955 Lugli, S., Manzi, V., Roveri, M., Schreiber, B.C., 2010. The Primary Lower Gypsum in the
956 Mediterranean: a new facies interpretation for the first stage of the Messinian salinity
957 crisis. Palaeogeography, Palaeoclimatology, Palaeoecology 297, 83–99.
958 Manzi, V., Roveri, M., Gennari, R., Bertini, A., Biffi, U., Giunta, S., Maria, S., Lanci, L.,
959 Lugli, S., Negri, A., Riva, A., Edoardo, M., Taviani, M., 2007. The deep-water
960 counterpart of the Messinian Lower Evaporites in the Apennine foredeep: The
961 Fanantello section (Northern Apennines, Italy). Palaeogeography, Palaeoclimatology,
962 Palaeoecology 251, 470–499.
963 Manzi, V., Gennari, R., Hilgen, F., Krijgsman, W., Lugli, S., Roveri, M., Sierro, F.J., 2013.
964 Age refinement of the Messinian salinity crisis onset in the Mediterranean. Terra
965 Nova 25, 315–322.
966 Manzi, V., Gennari, R., Lugli, S., Persico, D., Reghizzi, M., Roveri, M., Schreiber, B.C.,
967 Calvo, R., Gavrieli, I., Gvirtzman, Z., 2018. The onset of the Messinian salinity crisis
968 in the deep Eastern Mediterranean basin. Terra Nova 30, 189–198.

969 Mayser, J.P., Flecker, R., Marzocchi, A., Kouwenhoven, T.J., Lunt, D.J., Pancost, R.D.,
970 2017. Precession driven changes in terrestrial organic matter input to the Eastern
971 Mediterranean leading up to the Messinian Salinity Crisis. Earth and Planetary
972 Science Letters 462, 199–211.
973 Martinez-Ruiz, F., Kastner,M., Paytan, A., Ortega-Huertas,M., Bernasconi, S.M., 2000.
974 Geochemical evidence for enhanced productivity during S1 sapropel deposition in the
975 eastern Mediterranean. Paleoceanography 15, 200–209.
976 Marzocchi, A., Lunt, D.J., Flecker, R., Bradshaw, C.D., Farnsworth, A., Hilgen, F.J., 2015.
977 Orbital control on late Miocene climate and the North African monsoon: in-sight from
978 an ensemble of sub-precessional simulations. Climate of the Past 11, 1271–1295.
979 Meijer, P.Th., Tuenter, E., 2007. The effect of precession-induced changes in the
980 Mediterranean freshwater budget on circulation at shallow and intermediate depth.
981 Journal of Marine Systems 68, 349–365.
982 Modestou. S., Simon, D., Gutjahr, M., Marzocchi, A., Kowenhoven, T.J., Ellam, R.M.,
983 Flecker, R., 2017. Precessional variability of $^{87}Sr/^{86}Sr$ in the late Miocene Sorbas
984 Basin: an interdisciplinary study of drivers of interbasin exchange. Paleoceanography
985 32, 531–552.
986 Moller, T., Schulz, H., Hamann, Y., Dellwig, O., Kucera, M., 2012. Sedimentology and
987 geochemistry of an exceptionally preserved last interglacial S5 in the Levantine basin
988 (Mediterranean Sea). Marine Geology 291–294, 34–48.
989 Moore, D.M., Reynolds, R.C., 1997, X-ray diffraction and the identification and analysis of
990 clay minerals: New York, Oxford University Press, 378 p.
991 Mosca, P., Polino, R., Rogledi, S., Rossi, M., 2010. New data for the kinematic interpretation
992 of the Alps–Apennines junction (Northwestern Italy). International Journal of Earth
993 Sciences 99, 833–849.

994 Mussmann, M., Schulz, H.N., Strotmann, B., Kyær, T., Nielsen, L.P., Rossellò-Mora, R.A.,
995 Amann, R.I., Jørgensen, B.B., 2003. Phylogeny and distribution of nitrate-storing
996 *Beggiatoa* spp. in coastal marine sediments. Environmental Microbiology 5, 523–533.
997 Naafs, B. D. A., Hefter, J., Acton, G., Haug, G. H., Martínez-Garcia, A., Pancost, R., Stein,
998 R., 2012. Strengthening of North American dust sources during the late Pliocene (2.7
999 Ma). Earth and Planetary Science Letters 317, 8–19.
1000 Natalicchio, M., Dela Pierre, F., Lugli, S., Lowenstein, T.K., Feiner, S.J., Ferrando, S.,
1001 Manzi, V., Roveri, M., Clari, P., 2014. Did late Miocene (Messinian) gypsum
1002 precipitate from evaporated marine brines? Insights from the Piedmont Basin (Italy).
1003 Geology 42, 179–182.
1004 Natalicchio, M., Birgel, D., Peckmann, J., Lozar, F., Carnevale, G., Liu, X, Hinrichs, K.-U.,
1005 Dela Pierre, F., 2017. An archaeal biomarker record of paleoenvironmental change
1006 across the onset of the Messinian salinity crisis in the absence of evaporites (Piedmont
1007 Basin, Italy). Organic Geochemistry 113, 242–253.
1008 Negri, A., Giunta, S., Hilgen, F., Krijgsman, W., Vai, G.B., 1999. Calcareous nannofossil
1009 biostratigraphy of the Monte del Casino section (Northern Apennines, Italy) and
1010 paleoceanographic conditions at the times of late Miocene sapropel formation. Marine
1011 Micropaleontology 36, 13–30.
1012 Nesbitt, H., Young, G.M., 1982. Early Proterozoic climates and plate motions inferred from
1013 major element chemistry of lutites. Nature 299, 715–717.
1014 Nijenhuis, I.A., De Lange, G.J., 2000. Geochemical constraints on Pliocene sapropel
1015 formation in the eastern Mediterranean. Marine Geology 163, 41–63.
1016 Nijenhuis, I.A., Schenau, S.J., Van der Weijden, C.H., Hilgen, F.J., Lourens, L.J.,
1017 Zachariasse, W.J., 1996. On the origin of upper Miocene sapropelites: a case study
1018 from the Faneromeni section, Crete, Greece. Paleoceanography 11, 633–645.

1019 Ortiz, J.E., Moreno, L., Trinidad, T., Vegas, J., Ruiz-Zapata, B., Garćia-Cortés, Á., Galán, L.,
1020 Pérez-González, A., 2013. A 220 ka palaeoenvironmental reconstruction of the
1021 Fuenillejo maar lake record (Central Spain) using biomarker analysis. Organic
1022 Geochemistry 55, 85–97.
1023 Pancost, R.D., Boot, C.S., 2004. The palaeoclimatic utility of terrestrial biomarkers in marine
1024 sediments. Marine Chemistry 92, 239–261.
1025 Paytan, A., Griffith, E.M., 2007. Marine barite: recorder of variations in ocean export
1026 productivity. Deep-Sea Research II 54, 687–705.
1027 Perez-Folgado, M., Sierro, F.J., Barcena, M.A., Flores, J.A., Vazquez, A., Utrilla, R., Hilgen,
1028 F.J., Krijgsman, W., Filippelli, G.M., 2003. Western versus eastern Mediterranean
1029 paleoceanographic response to astronomical forcing: a high-resolution microplankton
1030 study of precession-controlled sedimentary cycles during the Messinian.
1031 Palaeogeography, Palaeoclimatology, Palaeoecology 190, 317–334.
1032 Poynter, J. Eglinton, G., 1990. Molecular composition of three sediments from Hole 717C:
1033 the Bengal Fan. In: Cochran, J.R, Stow, D.A.V et al. (Eds.), Proc. ODP, Sci. Results,
1034 116, College Station, TX (Ocean Drilling Program), 155–161.
1035 Reghizzi. M., Gennari, R., Douville, E., Lugli, S., Manzi, V., Montagna, P., Roveri, M.,
1036 Sierro, F.J., Taviani, M., 2017. Isotope stratigraphy ($^{87}Sr/^{86}Sr$, $\delta^{18}O$, $\delta^{13}C$) of the
1037 Sorbas basin (Betic Cordillera, Spain): paleoceanographic evolution across the onset
1038 of the Messinian salinity crisis, 2017. Palaeogeography, Palaeoclimatology,
1039 Palaeoecology 469, 60–73.
1040 Rohling, E.J., Marino, G., Grant, K.M., 2015. Mediterranean climate and oceanography and
1041 the periodic development of anoxic events (sapropels). Earth Science Reviews 143,
1042 62–97.

1043 Rommerskirchen, F., Eglinton, G., Dupont, L., Rullkötter, J., 2006. Glacial/interglacial
1044 changes in southern Africa: compound-specific $\delta^{13}C$ land plant biomarker and pollen
1045 records from southeast Atlantic continental margin sediments. Geochemistry
1046 Geophysics Geosystems 7, Q08010.
1047 Rossi, M., Mosca, P., Polino, R., Biffi, U., 2009. New outcrop and subsurface data in the
1048 Tertiary Piedmont Basin (NW Italy): unconformity bounded stratigraphic units and
1049 their relationships with basin modification phases. Rivista Italiana di Paleontologia e
1050 Stratigrafia 115, 305–335.
1051 Rossi, M., 2017. Outcrop and seismic expression of stratigraphic patterns driven by
1052 accommodation and sediment supply turnarounds: Implications on the meaning and
1053 variability of unconformities in syn-orogenic basins. Marine and Petroleum Geology
1054 87, 112–127.
1055 Roveri, M., Lugli, S., Manzi, V., Schreiber, B.C., 2008. The Messinian Sicilian stratigraphy
1056 revisited: new insights for the Messinian salinity crisis. Terra Nova 20, 483–488.
1057 Roveri, M., Flecker, R., Krijgsman, W., Lofi, J., Lugli, S., Manzi, V., Sierro, F.J., Bertini, A.,
1058 Camerlenghi, A., De Lange, G., Govers, R., Hilgen, F.J., Hübscher, C., Meijer, P.T.,
1059 Stoica, M., 2014. The Messinian Salinity Crisis: Past and future of a great challenge
1060 for marine sciences. Marine Geology 352, 25–58.
1061 Schefuß, E., Ratemeyer, V., Stuut, J.B.W, Jansen, H.F., Sinninghe Damsté, J.S., 2003.
1062 Carbon isotope analyses on *n*-alkanes in dust from the lower atmosphere over the
1063 central eastern Atlantic. Geochmica et Cosmochimica Acta 67, 1757–1767.
1064 Schenau, S.J., Antonarakou, A., Hilgen, F.J., Lourens, L.J., Nijenhuis, I.A., van det Weiden,
1065 C.H:, Zachariasse, W.J., 1999. Organic-rich layers from Metochia section (Gavdos,
1066 Greece): evidence for a single mechanism of sapropel deposition during the past 10
1067 My. Marine Geology 153, 117–135

1068 Schnetger, B., 1992. Chemical-composition of loess from a local and worldwide view. Neues
1069 Jahrbuch für Mineralogie-Monatshefte 1, 29–47.
1070 Schoepfer, S.-D., Shen, J., Wei, H., Tyson, R.W., Ingall, E., Algeo, T.J., 2015. Total organic
1071 carbon, organic phosphorous, and biogenic barium fluxes as proxies for paleomarine
1072 productivity. Earth-Science Reviews 149, 23–52.
1073 Schulz, H.N., Jørgensen, B.B., 2001. Big bacteria. Annuual Review of Microbiology 55,
1074 105–37.
1075 Schultz, L.G., 1964. Quantitative interpretation of mineralogical composition from X-ray and
1076 chemical data for the Pierre Shale. US Geological Survey Prof. Paper 391-C,
1077 Washington.
1078 Shepherd, T., Griffiths, W.D., 2006. The effects of stress on plant cuticular waxes. New
1079 Phytologist 171, 469–499.
1080 Sierro, F.J., Hilgen, F.J., Krijgsman, W., Flores, J.A., 2001. The Abad composite (SE Spain):
1081 a Messinian reference section for the Mediterranean and the APTS. Palaeogeography,
1082 Palaeoclimatology, Palaeoecology 168, 141–169.
1083 Sierro, F.J., Flores, J.A., Frances, G., Vazquez, A., Utrilla, R., Zamarreno, I., Erlenkeuser, H.,
1084 Barcena, M.A., 2003. Orbitally-controlled oscillations in planktic communities and
1085 cyclic changes in western Mediterranean hydrography during the Messinian.
1086 Palaeogeography, Palaeoclimatology, Palaeoecology 190, 289–316.
1087 Simon, D., Marzocchi, A., Flecker, R., Lunt, D.J., Hilgen, F.J., Meijer, P.T., 2017.
1088 Quantifying the Mediterranean freshwater budget throughout the late Miocene: new
1089 implications for sapropel formation and the Messinian salinity crisis. Earth and
1090 Planetary Science Letters 472, 25–37.

1091 Sinninghe Damsté, J.S., Kenig, F., Koopmans, M.P., Köster, J., Schouten, S., Hayes, J.M., de
1092 Leeuw, J.W., 1995. Evidence for gammacerane as an indicator of water column
1093 stratification. Geochimica et Cosmochimica Acta 59, 1895–1900.
1094 Sinninghe Damsté, Kuypers, M.M.M., Schouten, S., Schulte, S., Rullkötter, J., 2003. The
1095 lycopene/C_{31} *n*-alkane ratio as a proxy to assess palaeoxicity during sediment
1096 deposition. Earth and Planetary Science Letter 209, 215–226.
1097 Sturani, C., 1973. A fossil eel (*Anguilla* sp.) from the Messinian of Alba (Tertiary Piedmont
1098 Basin). Palaeoenvironmental and palaeogeographic implications, In: Drooger C.W.
1099 (Ed.), Messinian events in the Mediterranean. K. Nederl. Akad. Wetensch.,
1100 Amsterdam, 243–255.
1101 Taylor, G.T., Iabichella, M., Ho, T.Y, Scranton, M.I, Thunnell, R.C., Karger, M., Varela, R.,
1102 2001. Chemoautotrophy in the redox transition zone of the Cariaco Basin: a
1103 significant midwater source of organic carbon production. Limnology and
1104 Oceanography 46, 148–163.
1105 Tomadin, L., 2000. Sedimentary fluxes and different dispersion mechanisms of the clay
1106 sediments in the Adriatic Basin. Rendiconti Lincei 11, 161–174.
1107 Tomadin, L., Lenaz, R., 1989. Eolian dust over the Mediterranean and their contribution to
1108 the present sedimentation. In: Leinen M., Sarnthein M. (Eds.), Paleoclimatology and
1109 paleometeorology: modern and past patterns of global atmospheric transport. Kluwer,
1110 Dordrecht, 267–282.
1111 Tomadin, L., Lenaz, R., Landuzzi, V., Mazzucotelli, A., Vannucci, R., 1984. Wind-blown
1112 dusts over the Central Mediterranean. Oceanologica Acta *7*, 13–23.
1113 Toucanne, S., Minto' C.M.A., Fontanier, C., Bassetti, M.A., Jorry, S.J., Jouet, G. , 2015.
1114 Tracking rainfall in the northern Mediterranean borderlands during sapropel
1115 deposition. Quaternay Science Reviews 129, 178–195.

van der Laan, E., Hilgen, F.J., Lourens, L.J., de Kaenel, E., Gaboardi, S., Iaccarino, S., 2012. Astronomical forcing of Northwest African climate and glacial history during the late Messinian (6.5–5.5 Ma). Palaeogeography, Palaeoclimatology, Palaeoecology 313, 107–126.

Van Os, B.J.H., Lourens, L.J., Hilgen, F.J., De Lange, G.J., Beaufort, L., 1994. The formation of Pliocene sapropels and carbonate cycles in the Mediterranean: diagenesis, dilution and productivity. Paleoceanography 9, 601–617.

Vazquez, A., Utrilla, R., Zamarreno, I., Sierro, F.J., Flores, J.A., Francés, G., Bàrcena M.A., 2000. Precession-related sapropelites of the Messinian Sorbas Basin (South Spain): paleoenvironmental significance. Palaeogeography, Palaeoclimatology, Palaeoecology 158, 353–370.

Violanti, D., Gallo, L.M., Rizzi, A., 2007. Foraminiferal assemblages of the Bric della Muda laminites (Nizza Monferrato, Piedmont): proxies of cyclic paleoenvironmental changes in the lower Messinian of North-Western Italy. Geobios 40, 281-290.

Violanti, D., Lozar, F., Natalicchio, M., Dela Pierre, F., Bernardi, E., Clari, P., Cavagna, S., 2013. Stress-tolerant microfossils of a Messinian succession from the Northern Mediterranean basin (Pollenzo section, Piedmont, northwestern Italy). Bollettino della Società Paleontologica Italiana 52, 45–54.

Wakeham, S.G., Amann, R., Freeman, K.H., Hopmans, E.C., Jørgensen, B.B., Putnam, I.F., Schouten, S., Sinninghe Damsté, J.S., Talbot, H.M., Woebken, D., 2007. Microbial ecology of the stratified water column of the Black Sea as revealed by a comprehensive biomarker study. Organic Geochemistry 38, 2070–2097.

Wehausen, R., Brumsack, H.J., 1998. The formation of Pliocene Mediterranean sapropels: constraints from high-resolution major and minor element studies. In: Robertson,

A.H.F., Emeis, K.-C., Richter, C., Camerlenghi, A. (Eds.), Proc. ODP, Sci. Results, 160, College Station, TX (Ocean Drilling Program), 207–217.

Wehausen, R., Brumsack, H.J., 1999. Cyclic variations in the chemical composition of eastern Mediterranean Pliocene sediments: a key for understanding sapropel formation. Marine Geology 153, 161–176.

Wehausen, R., Brumsack, H.J., 2000. Chemical cycles in Pliocene sapropel-bearing and sapropel-barren eastern Mediterranean sediments. Palaeogeography, Palaeoclimatology, Palaeoecology 158, 325–352.

Wilkin, R.T., Barnes, H.L., Brantley, S.L., 1996. The size and distribution of framboidal pyrite in modern sediments: an indicator of redox conditions. Geochimica et Cosmochimica Acta 60, 3897–3912.

Willet, S.D., Schlunneger, F., Picotti, V., 2006. Messinian climate change and erosional destruction of the central European Alps. Geology 34, 613–616.

Zhao, Y., Colin, C., Liu, Z., Bonneau, L., Siani, G., 2016. Climate forcing of terrigenous sediment input to the central Mediterranean Sea since the early Pleistocene. Palaeogeography, Palaeoclimatology, Palaeoecology 442, 23–35.

Captions

Fig. 1:

A) Distribution of the Messinian evaporites in the Mediterranean Basin (modified from Manzi et al., 2013; PB: Piedmont Basin). B) Structural sketch map of the Piedmont Basin (PB; modified from Bigi et al., 1990). TH: Torino Hill; MO: Monferrato; gray dotted lines indicate the isobaths of the base of Pliocene. C) Sketch showing the lateral transition from

1165 marginal gypsum deposits (Primary Lower Gypsum unit ; Arnulfi section) to cyclic
1166 sequences of organic-rich shales (dark gray), marls, and carbonate-rich deposits (light gray)
1167 in the deeper part of the basin (Pollenzo section). PLG: Primary Lower Gypsum; SAF:
1168 Sant'Agata Fossili marls; MSC: Messinian salinity crisis. (modified from Dela Pierre et al.,
1169 2011). The ages of the PLG cycles are from Manzi et al. (2013).
1170
1171 **Fig. 2:**
1172 Correlation of the Pollenzo section with the astronomically-tuned (65°N summer insolation
1173 and eccentricity curve; Laskar et al., 2004) Perales reference section (Spain; modified from
1174 Manzi et al., 2013). LO: last occurrence. LR PF: last recovery of planktic foraminifers. CN:
1175 calcareous nannofossils. PLG: Primary Lower Gypsum; MSC: Messinian salinity crisis;
1176 SKB: Sturani Key Bed (modified from Lozar et al., 2018).
1177
1178
1179 **Fig. 3:**
1180 A) The Pollenzo section, with locations of the studied samples and their corresponding
1181 calcium carbonate ($CaCO_3$) contents. B) Outcrop view of the shales of cycle Pm5: olive gray,
1182 laminated shales are interbedded with light gray silty layers, locally showing normal grading.
1183 C) Bioturbated marls of cycle Pm5; burrows are indicated by arrows. D) Laminated marls of
1184 cycle Pm7, hosting a carbonate-rich bed (f). E) Detail of D, showing fine lamination, defined
1185 by alternation of gray and whitish laminae. F) Laminated beds including a whitish layer of
1186 cycle Pg1. The ages of cycles are from Manzi et al. (2013).
1187
1188 **Fig. 4:**

A) Polished slab cut perpendicular to bedding of shales of cycle Pm6: note lamination defined by alternation of whitish and darker laminae; a massive silty layer is present in the lower part of the image. B) Polished slab of a whitish lamina cut parallel to bedding from the layer shown in A); note the irregularly-shaped whitish aggregates, probably corresponding to marine "snow" floccules (arrows). C, D) Photomicrographs in transmitted (C) and UV light (D) of the shales of cycle Pm6. Note the graded, terrigenous layer (arrow) in (C) and the bright, organic-rich laminae rich in peloids in (D). The dark elongated clast in the upper left corresponds to a phosphatic fish remain. The inset in (C) is a backscatter SEM image of a dwarf planktic foraminifer (sample Pm6_4.2). E), F) Photomicrographs in transmitted light of fecal pellets (arrows) in the shale of cycle Pm7. G), H) Slabs cut parallel to bedding (G fresh cut; H polished slab) of the laminated marls of cycles Pm6 and Pg1, showing dense mazes of filamentous microfossils. I) UV light photomicrograph of the laminated marls, with autofluorescent filamentous microfossils. Detail with enlarged filaments is shown in the inset.

Fig. 5:

A) Back scatter SEM image of a mold of a centric diatom in the shales of cycle Pm6. B) SEM image of a fecal pellet composed of coccoliths engulfed in a silica-rich matrix (cycle Pm5). Detail in the inset. C) Back scatter SEM image of the shales of cycle Pm6; the light grains are pyrite framboids. Detail of a framboid is shown in the inset. D) Back scatter SEM image of the laminated marls of cycle Pm6, showing the contact between laminae rich (below) and poor (above) in terrigenous particles. E) SEM image of a curved filament (arrow) from the laminated marls of cycle Pg1. F) SEM image of roundish dolomite microcrystals on the outer surface of a filamentous microfossil. Some crystals display a hollow core (arrows).

Fig. 6:

Element/aluminum (Al) ratios of the Pollenzo section. Gray shaded bars indicate bioturbated and laminated marls. For key to lithologies see Fig. 3. The ages of cycles are from Manzi et al. (2013).

Fig. 7:

TOC (%) content, *n*-alkane distribution (μg/g TOC), ratios of *n*-alkanes (ACL), and compound-specific carbon isotope values ($\delta^{13}C$) of specific *n*-alkanes of the Pollenzo section. Gray shaded bars indicate bioturbated and laminated marls. alk: alkanes; CPI: Carbon Preference Index; ACL: Average Chain Length. For key to lithologies see Fig. 3. The ages of cycles are from Manzi et al. (2013).

Fig. 8:

Gas chromatograms (*m/z* 71) of *n*-alkanes from three selected samples of laminated marls (top), shales (center), and bioturbated marls (bottom). Black triangles: *n*-alkanes with odd carbon numbers; black dots: *n*-alkanes with even carbon numbers. Note that the shale sample (Pm5_1.5) contains more *n*-alkanes with even carbon number than the other lithologies (marls), resulting in a lower CPI (Carbon Preference Index) value. C_{35}-Lyc: coelution of *n*-C_{35}-alkane and lycopane.

Fig. 9:

Plot of the carbon preference index (CPI) and *n*-$C_{29\text{-}33}$ alkane $\delta^{13}C$ values. The green, purple, and orange rectangles enclose clusters of shale, laminated, and bioturbated marl samples,

1238 respectively. Green and light brown shades indicate the range of $\delta^{13}C$ values of C_3 and C_4
1239 plants, respectively.
1240
1241 **Fig. 10:**
1242 Plots of the Ti/Al (A) and Zr/Al ratios (B) versus total Al_2O_3 contents in the studied
1243 Messinian samples and comparison with chemical compositions of Pliocene sapropels
1244 (Wehausen and Brumsack, 1998) and Pleistocene to recent Po River sediments (Amorosi et
1245 al., 2002). The Al_2O_3 contents of the Pollenzo shales (green triangles) plot in the field of Po
1246 river sediments. C) Plot of K/Al and Mg/Al ratios (triangles: shales; circles: bioturbated
1247 marls; squares: laminated marls). Samples with very high Mg/Al ratios (>100) from cycles
1248 Pm7 and Pg1 are excluded because of the presence of dolomite. Saharan dust composition is
1249 from Wehausen and Brumsack (1998). The black arrows indicate a trend of increased aeolian
1250 input.
1251
1252 **Fig. 11:**
1253 Clay mineral compositions and relative abundance of shales (sample Pm6_4.1) and
1254 bioturbated marls (sample Pm6_1.1).
1255
1256 **Fig. 12:**
1257 Sketch showing the climate-controlled paleoenvironmental changes affecting the studied
1258 marginal Mediterranean basin across the MSC onset (see text for explanations). A) Shale
1259 deposition during humid phases at precession minima (insolation maxima) before and after
1260 the MSC onset. B), C) Deposition of bioturbated marls (B) and laminated marls (C) during
1261 arid phases at precession maxima (insolation minima). Blue arrows indicate freshwater (thin

arrow) and seawater (thick arrow) inputs. Blue dashed arrows indicate water mixing. Brown arrows indicate aeolian transport. P: Pollenzo section.

Supplementary Table 1:

TOC and major and trace element contents of the studied samples.

Supplementary Table 2:

n-alkane relative abundances, ratios, and carbon isotope composition of the studied samples.

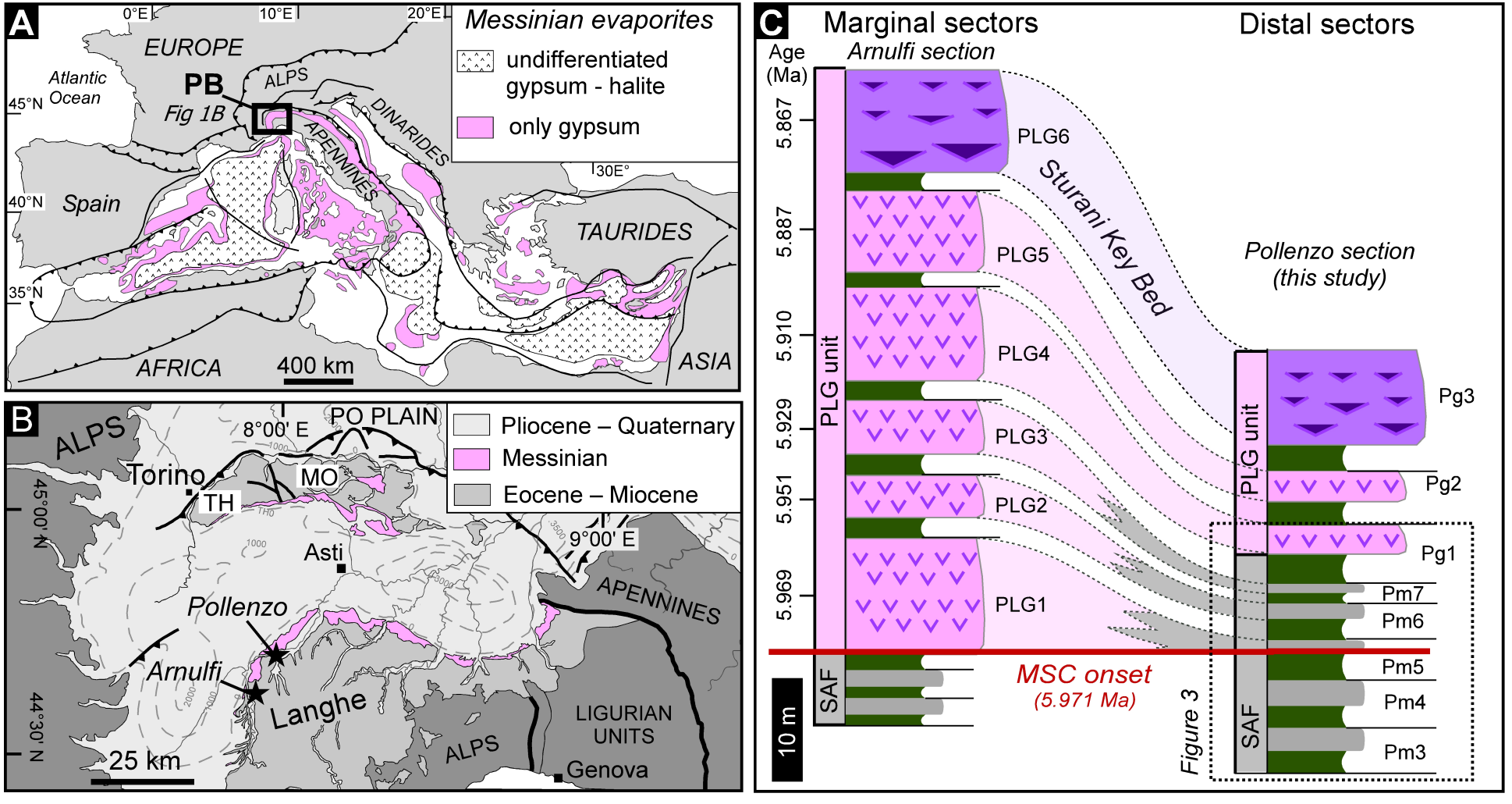

Natalicchio et al., Fig. 1_P3_rev

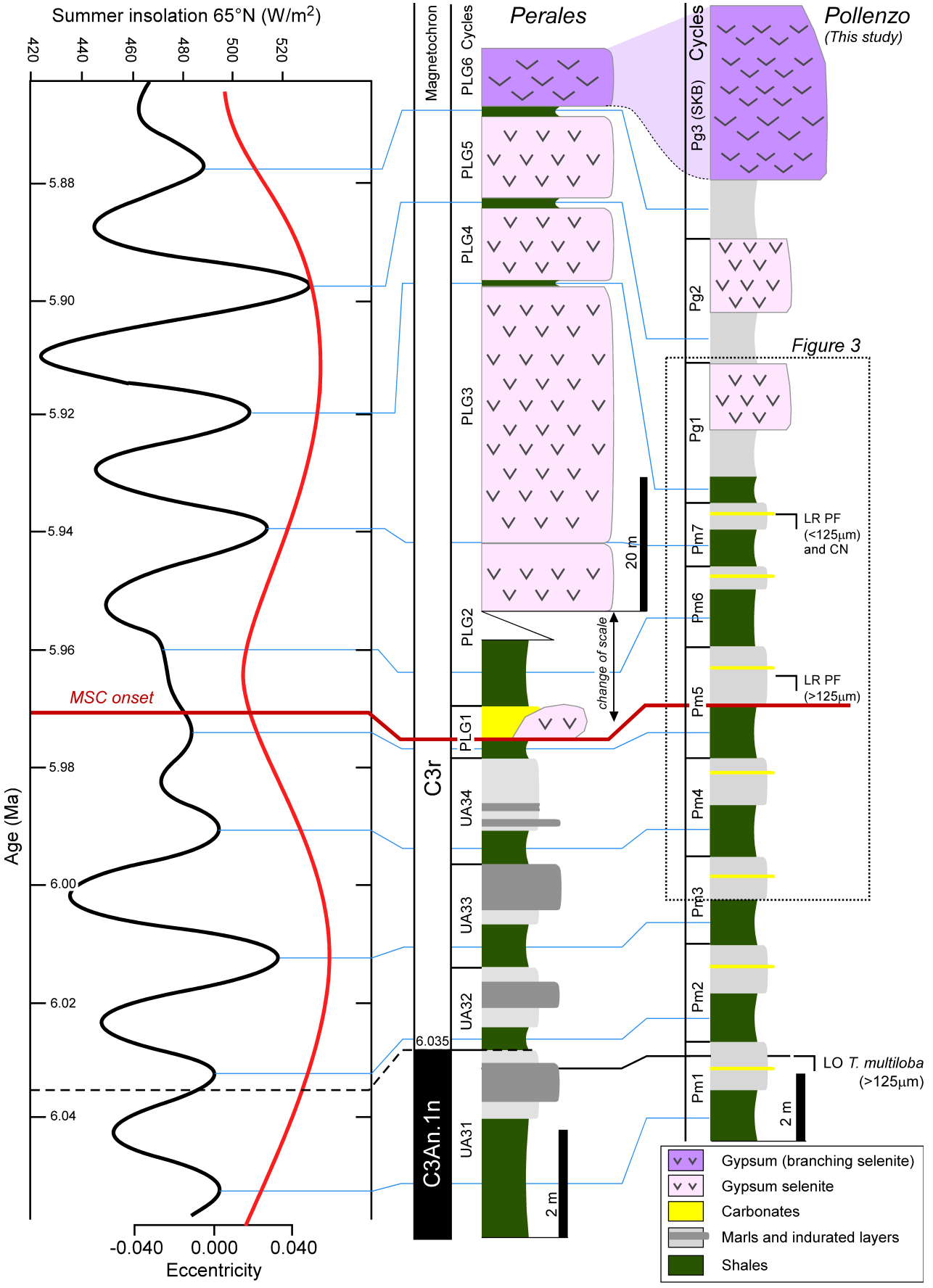

Natalicchio et al., Fig. 2_P3_rev

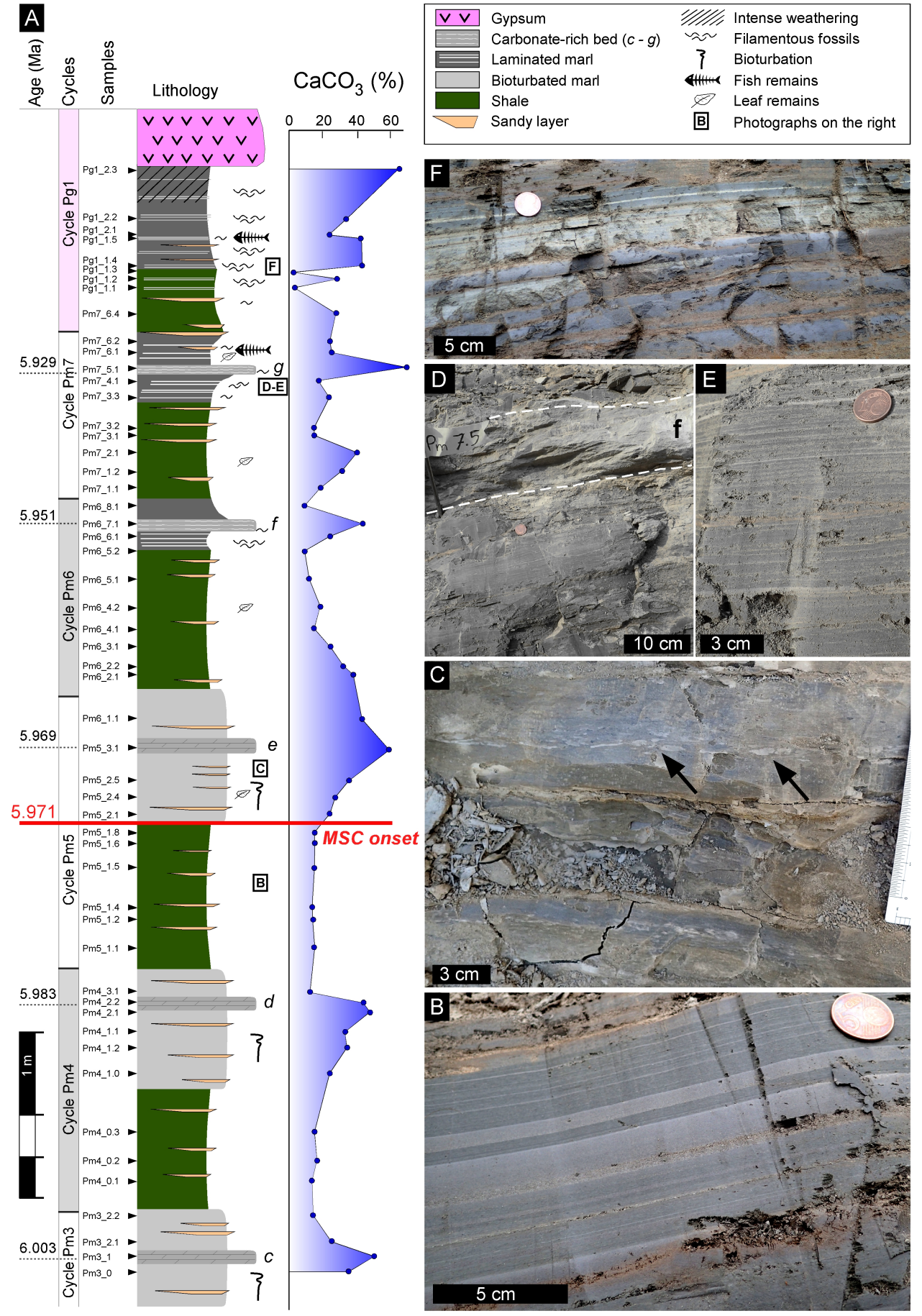

Natalicchio et al. Fig.3_P3_rev

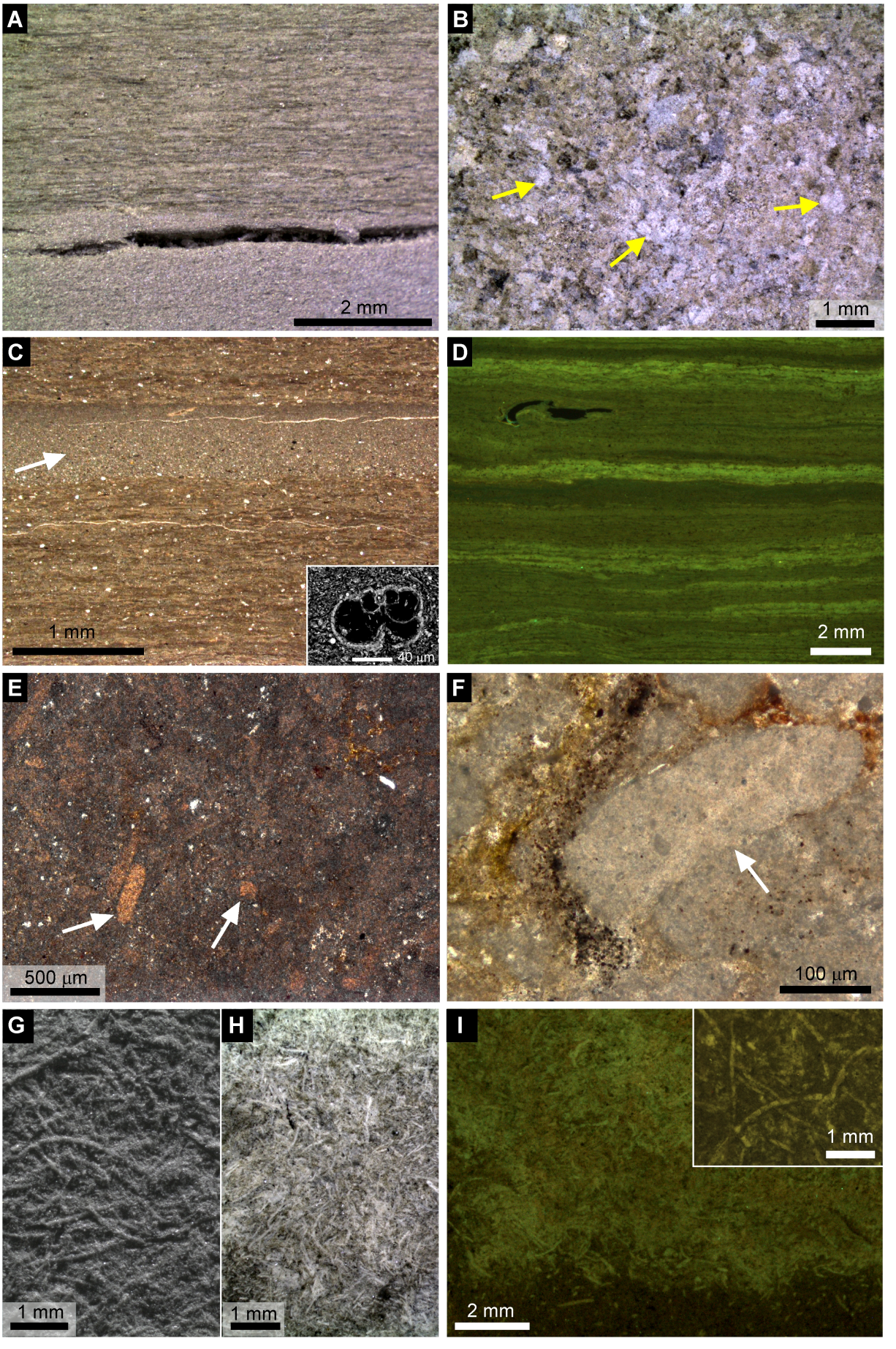

Natalicchio et al Fig. 4_P3

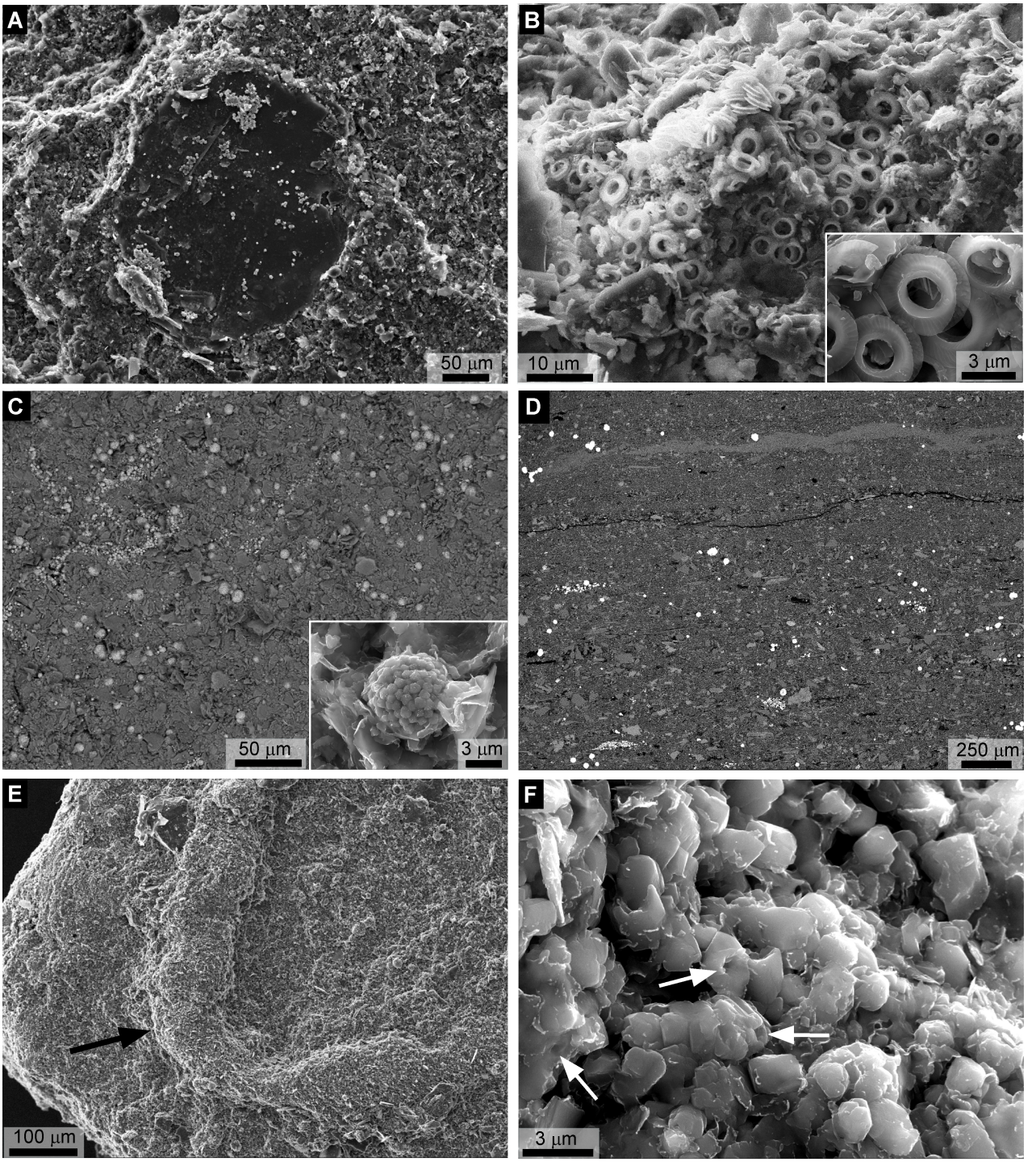

Natalicchio et al Fig. 5_P3

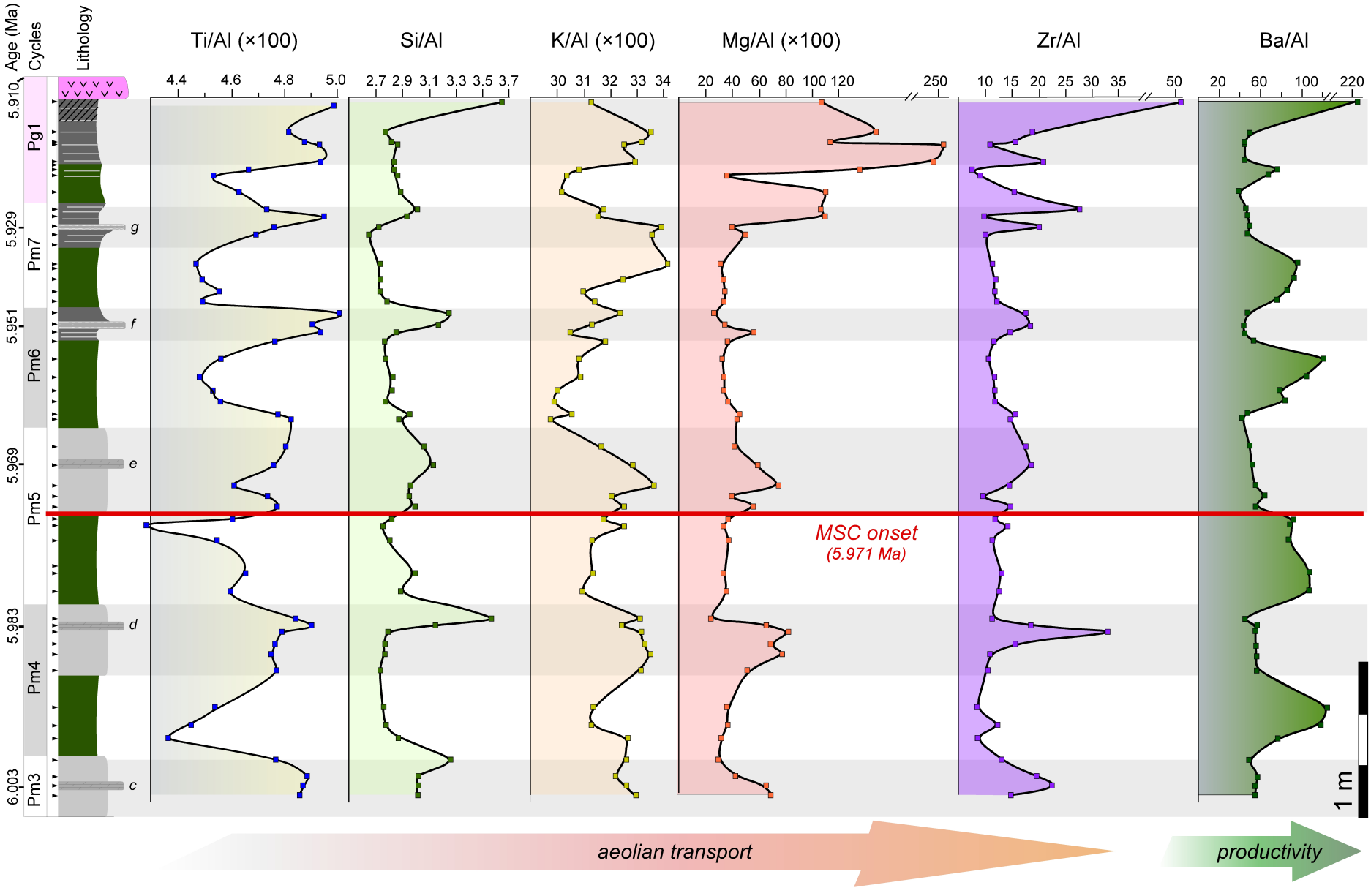

Natalicchio et al. FIG. 6_P3_rev

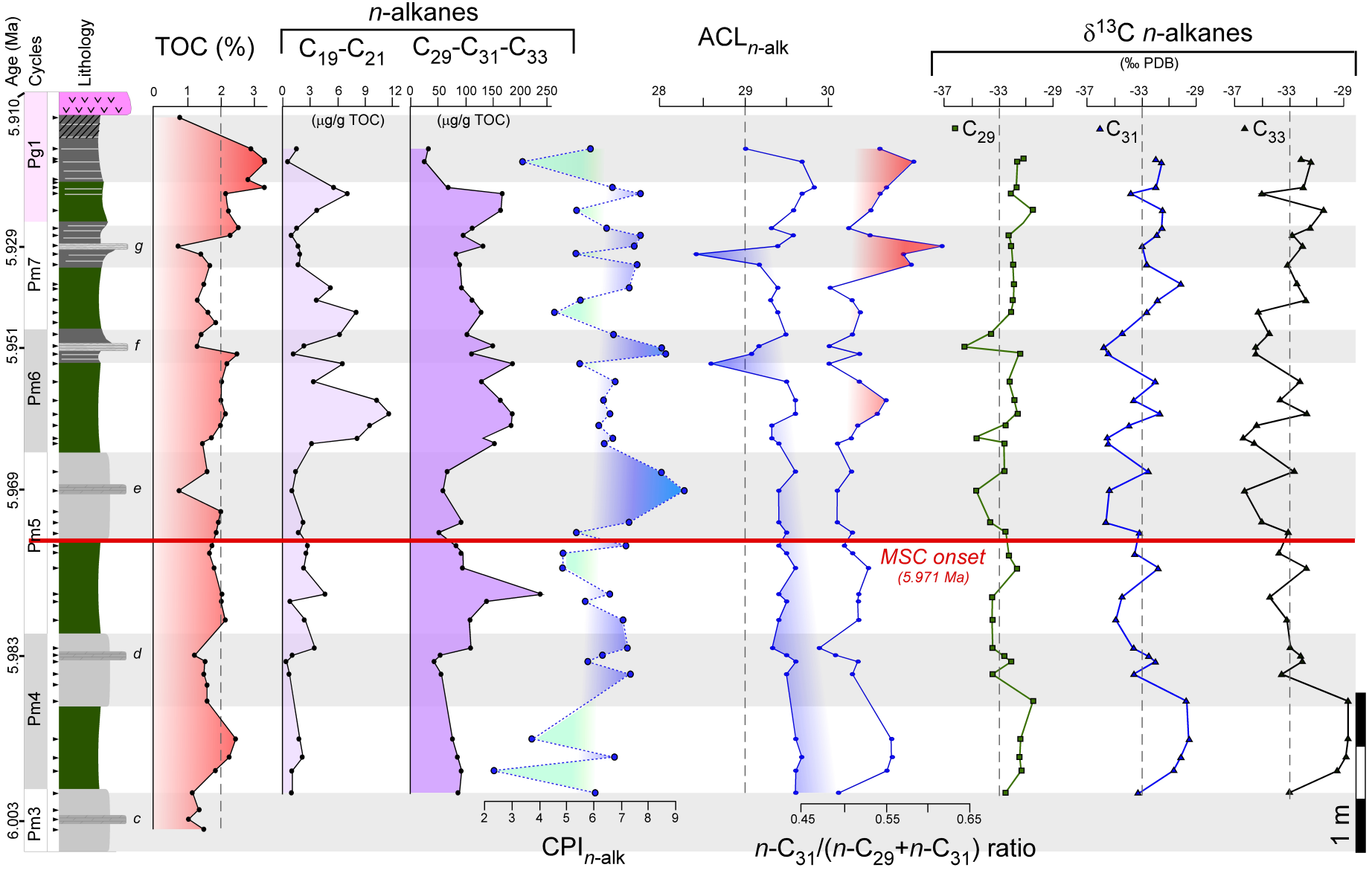

Natalicchio et al. FIG. 7_P3_rev

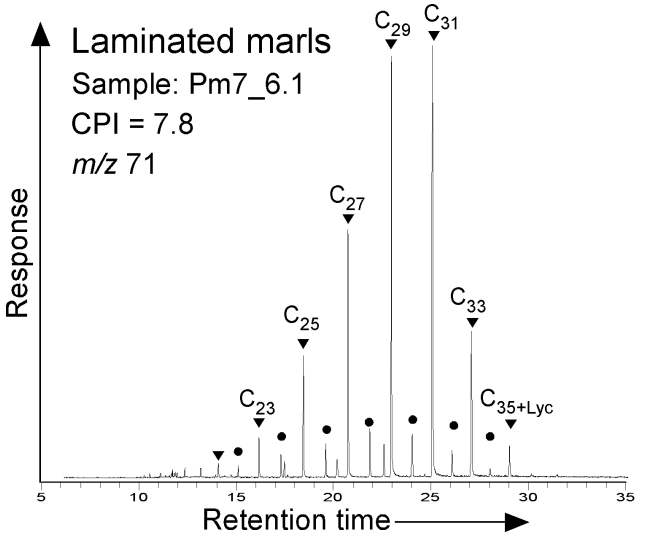

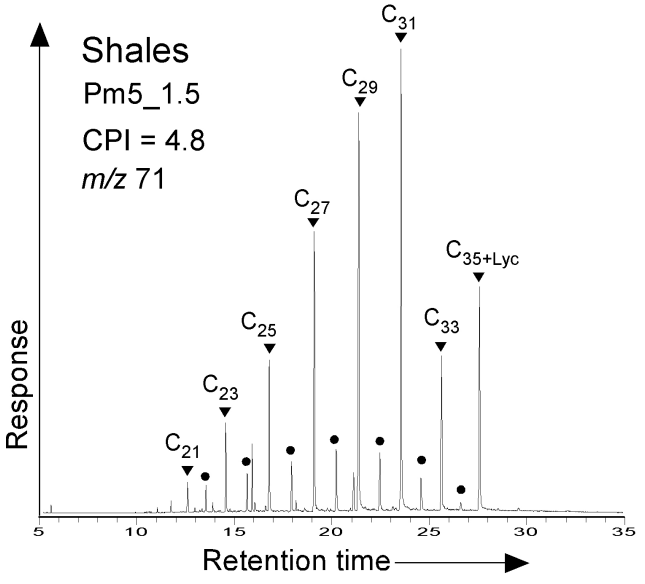

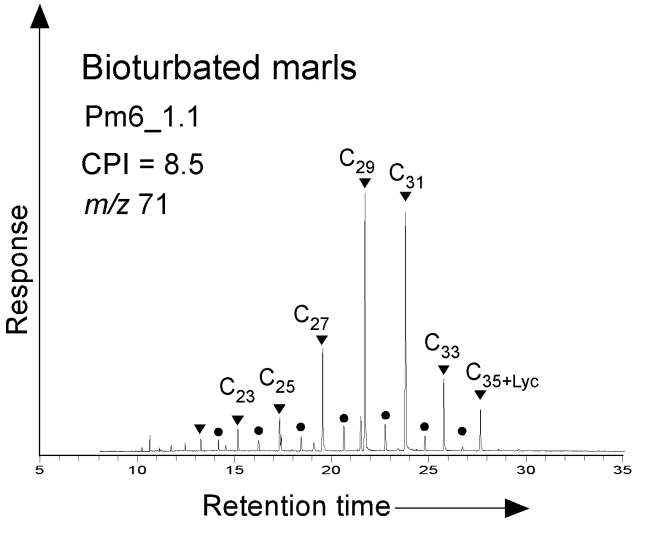

Natalicchio et al Fig. 8_P3

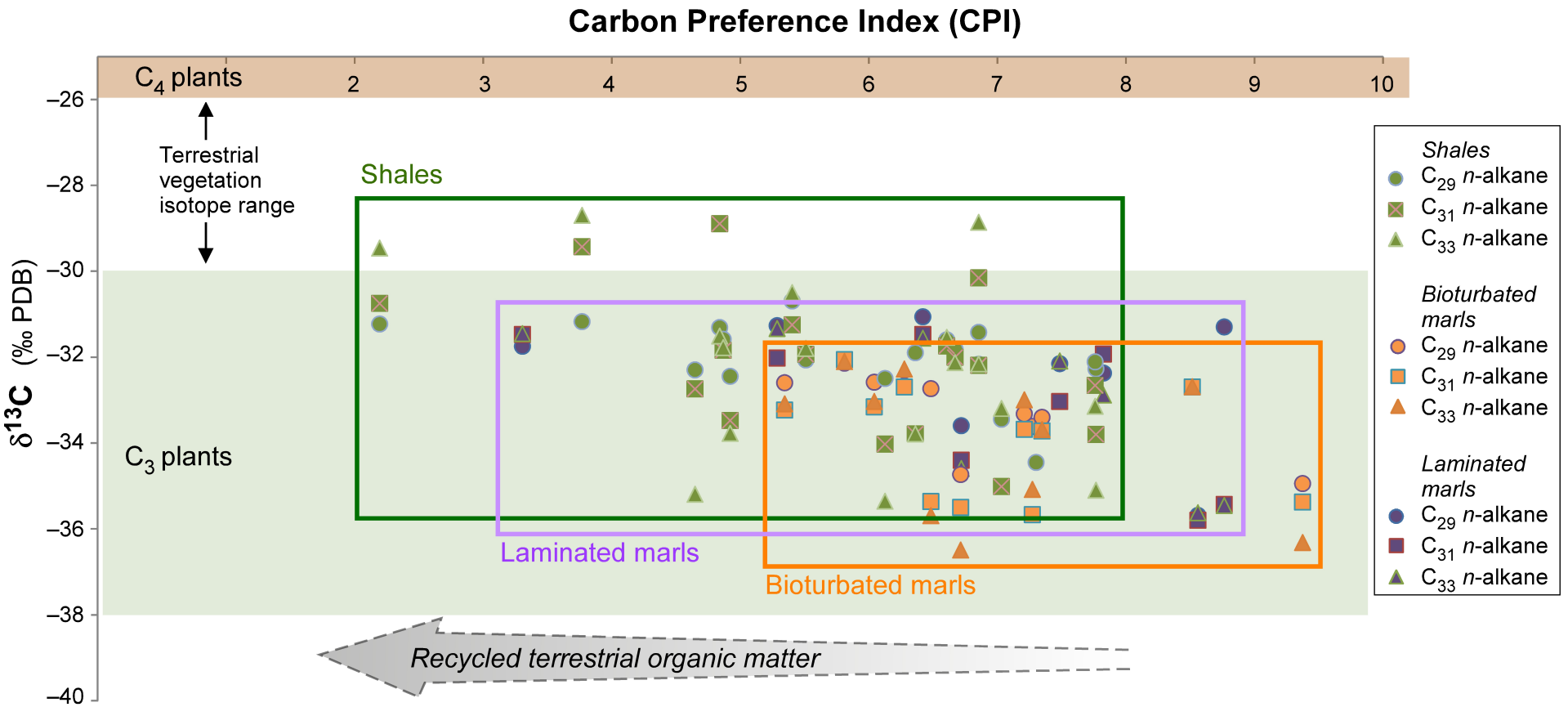

Natalicchio et al Fig. 9_P3

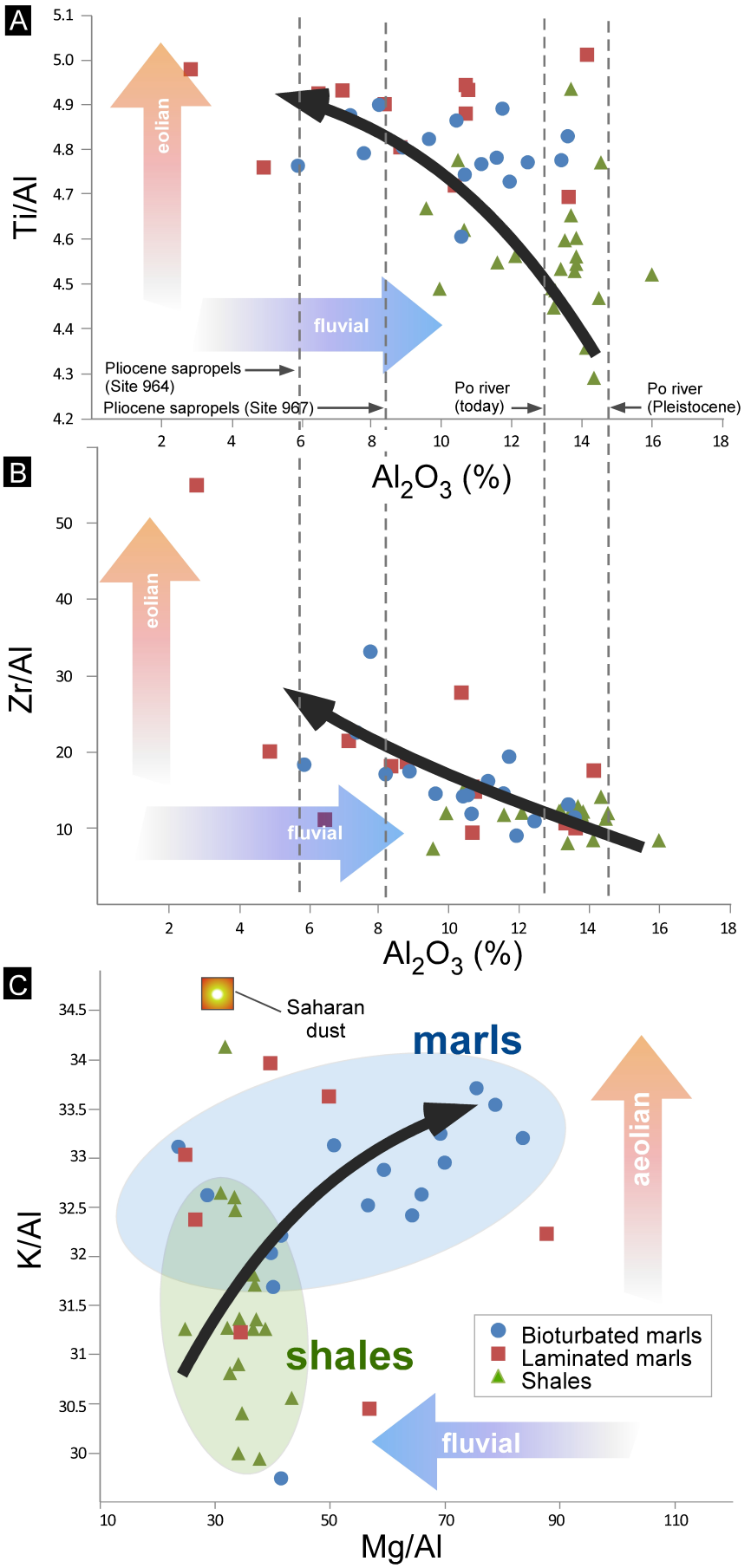

Natalicchio et al Fig.10_P3_rev

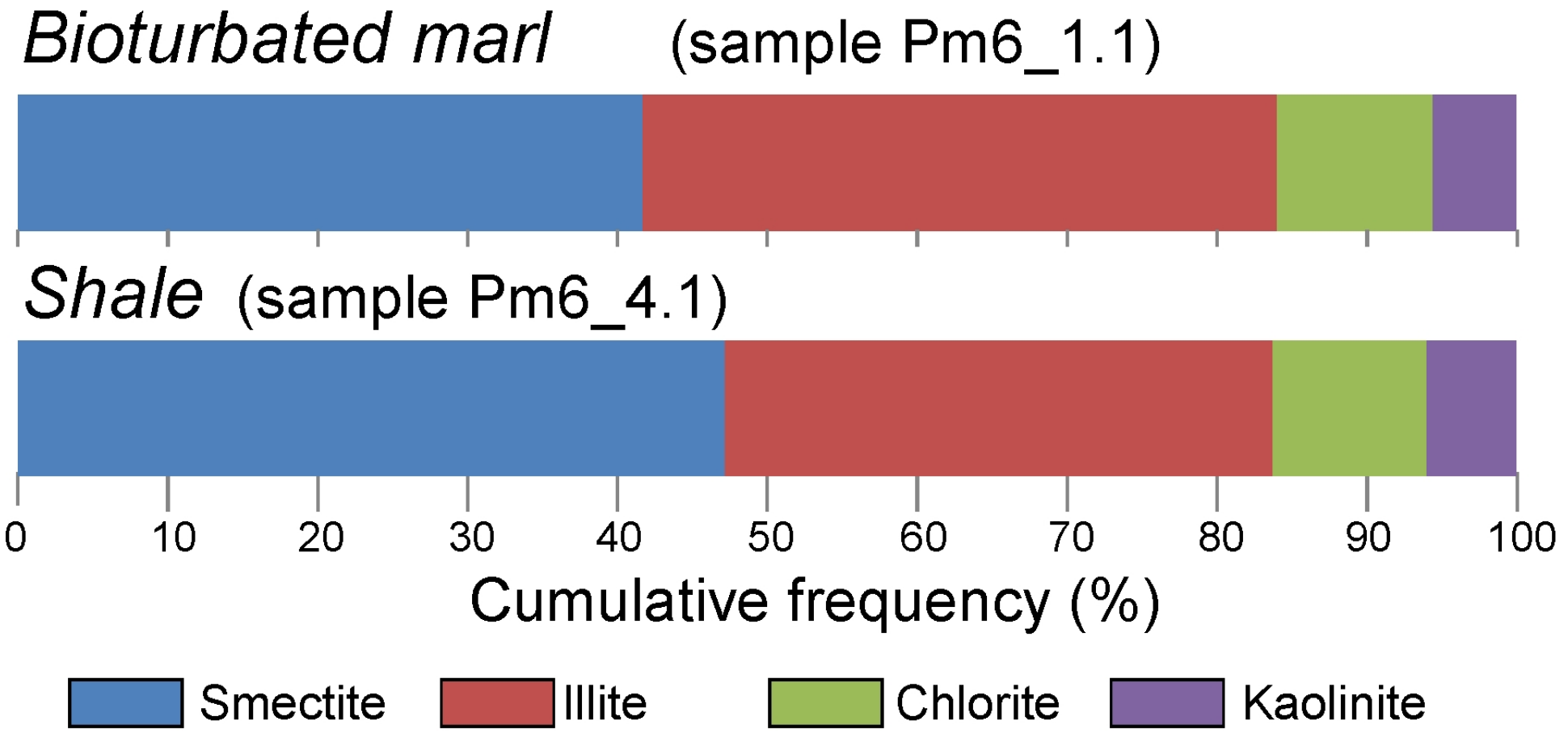

Natalicchio et al., Fig. 11_P3

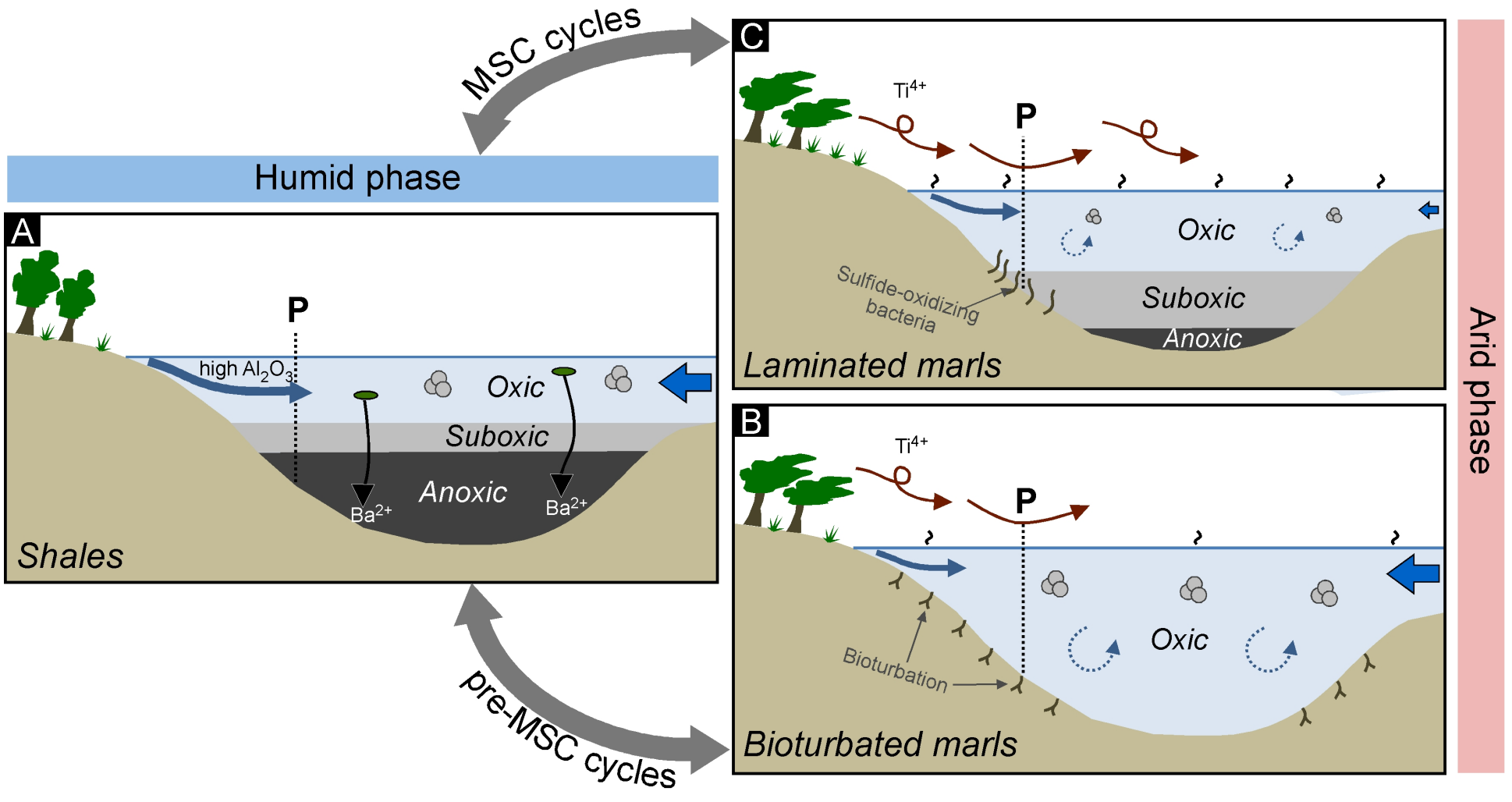

Natalicchio et al. Fig. 12_P3